Computational Mechanics
https://doi.org/10.1007/s00466-026-02772-z

ORIGINAL PAPER

A new generalized displacement control for nonlinear spectral stochastic finite element problems

Lukas Panther[1] · **Werner Wagner**[1] · **Steffen Freitag**[1]

Received: 8 November 2025 / Revised: 2 February 2026 / Accepted: 20 February 2026

Abstract
The influence of uncertain material parameters on the mechanical behavior of structures is investigated using stochastic structural analysis. A widely used method for estimating the stochastic characteristics of the structural response is the Monte Carlo simulation (MCS). However, this approach exhibits a slow convergence rate. In this paper, we investigate geometrically nonlinear finite element problems using the spectral stochastic finite element method (SSFEM). This application of the SSFEM remains comparatively unexplored to date, see [1, 2, 14]. The SSFEM combines the polynomial chaos expansion (PCE) with the finite element method (FEM). The basis of the SSFEM is an extended variational formulation, which is discretized in the stochastic domain using the PCE and in the spatial domain using the FEM. This paper focuses on the development and implementation of solution algorithms for tracing nonlinear equilibrium paths within the framework of the SSFEM. In addition to existing standard solution methods, a generalized displacement control is developed for the application within the SSFEM. This algorithm allows the investigation of mechanical problems that cannot be solved using standard solution methods. The applicability of the developed solution algorithm is demonstrated through three numerical examples involving different structural elements. Besides a shell formulation similar to [13], a mixed-hybrid two-dimensional solid element and a geometrically exact beam element are used, see [12]. Furthermore, the implementation of the SSFEM into a general finite element program is shown. All algorithms required for implementing a geometrically nonlinear spectral stochastic FE formulation for a two-dimensional solid element are provided in the appendices.

Keywords Solution algorithms · Generalized displacement control · Nonlinear spectral stochastic FEM · Polynomial chaos expansion · Uncertainty quantification

1 Introduction

Lightweight and thin-walled structures are widely used in technical applications due to their outstanding properties. However, their slenderness makes them prone to instabilities, such as snap-through behavior. Moreover, these structures are often subject to large deformations. To analyze their load–displacement behavior in finite element simulations, geometrically nonlinear FE formulations are mandatory. Furthermore, appropriate path-following algorithms are required to trace the nonlinear equilibrium path of the structure under consideration.

The response of structures exhibiting instabilities and large deformations is highly sensitive to variations in their material properties. These parameters are subject to inherent randomness, commonly referred to as aleatoric uncertainty. To model this type of uncertainty, either random variables or spatially correlated random fields are typically used. Within stochastic structural analysis, the influence of uncer-

✉ Werner Wagner
werner.wagner@kit.edu

✉ Steffen Freitag
steffen.freitag@kit.edu

Lukas Panther
lukas.panther@kit.edu

[1] Institute for Structural Analysis, Karlsruhe Institute of Technology (KIT), Kaiserstr. 12, 76131 Karlsruhe, Germany

Published online: 21 May 2026

tain parameters on the mechanical behavior of geometrically nonlinear structures is investigated.

After propagating the uncertain parameters through the computational model, the statistics of a quantity of interest can be calculated. These quantities may include a specific displacement or stress component, a reaction force, or a load factor. A commonly used method in stochastic analysis is the Monte Carlo simulation. The MCS is used to estimate stochastic attributes, such as the mean value, standard deviation, and higher-order moments. However, this approach suffers from a slow convergence rate [6].

An efficient approach to consider uncertainties within a FE simulation is the spectral stochastic finite element method, which was first proposed by [8] in the 1990s. The SSFEM combines the polynomial chaos expansion with the finite element method and represents an extension of the conventional FEM. The development of stochastic FE formulations is based on an extended variational formulation, which is discretized in the spatial dimension by means of the FEM and in the stochastic dimension using the PCE. Originally developed by [26] for normal distributions, the PCE was later extended to arbitrary probability distributions by [28, 29]. Due to the intrusive nature of the SSFEM, various arithmetic operations, such as multiplication and division of two PC expansions, are required, see [7].

An overview of the SSFEM and its applications in various research areas is provided, e.g., in [3, 18]. While the method has been extensively applied to linear problems in solid mechanics, its extension to geometrically nonlinear problems remains comparatively unexplored. This applies both to FE formulations for d and to suitable path-following algorithms for tracing the nonlinear equilibrium path of a mechanical structure.

In [1], the SSFEM is applied for the first time to problems involving finite deformations. The effect of a random spatial domain is examined using a tensile specimen. Additionally, the influence of a random fiber orientation in a composite material on the structural response of the tensile specimen is investigated. A geometrically exact co-rotational beam formulation for the application within the SSFEM is proposed by [14]. The authors investigate the behavior of different structures under a spatially correlated random Young's modulus, including a shallow truss structure and an arched beam. Reference [2] further addresses geometrically nonlinear problems within the framework of the SSFEM, such as the buckling behavior of a beam.

In [14], two standard solution algorithms, namely the load control and the single displacement control, are described, and their application within the context of the SSFEM is briefly discussed. The first solution method, however, has very limited applicability, particularly for stability problems. In contrast, the latter solution algorithm can trace the complete equilibrium path when a structure snaps through. Nevertheless, this method has certain limitations regarding the applied external load. The present work aims to develop a suitable solution algorithm within the SSFEM to overcome the limitations identified above.

Therefore, we propose a generalized displacement control within the framework of the SSFEM, extending the original algorithm from [4, 25]. This solution method allows the calculation of SSFEM problems that cannot be investigated with existing algorithms. The highlights of the present paper can be summarized as follows:

- Development of a generalized displacement control within the framework of the SSFEM,
- Detailed flowchart of the proposed solution algorithm for the implementation into a general finite element (FE) program,
- Consistent linearization of all relationships within the proposed solution algorithm,
- Illustration of the seamless connection between the stochastic and deterministic formulas of the generalized displacement control,
- Application of the proposed solution algorithm together with different spectral stochastic FE formulations to challenging numerical examples,
- Provision of vectorized implementations for several arithmetic operations involving PC expansions,
- Detailed element framework including all subroutines required to implement a geometrically nonlinear two-dimensional solid element.

The paper is organized as follows. In Sect. 2, the representation of random variables using the PCE is briefly summarized. The main steps of the two-step discretization scheme with the PCE and the FEM of the linearized variational principle are described in Sect. 3. Section 4 reviews standard solution algorithms, such as the load and the single displacement control in the context of the SSFEM, including illustrative examples. The generalized displacement control developed in this paper is presented in Sect. 5. This section also concludes with an illustrative example. Section 6 provides an overview of how the SSFEM is implemented into a general finite element program. In Sect. 7, the proposed solution algorithm is applied together with different spectral stochastic FE formulations to challenging numerical examples. The discretization of random fields and their representation with the PCE is briefly summarized in Appendix A. In Appendix B, we provide vectorized implementations of arithmetic operations with PC expansions. A detailed element framework for a geometrically nonlinear two-dimensional solid element is given in Appendix C.

2 Random variables and polynomial chaos expansion

Let $(\Omega, \Sigma, \mathbb{P})$ be the probability space, where Ω is the event space, Σ the σ-algebra on Ω and $\mathbb{P}$ the probability measure on (Ω, Σ). Within the probability theory, the mapping from the probability space to the set of real numbers $\mathbb{R}$ is given by the random variable

$$X(\omega): \ \Omega \mapsto D_X \subset \mathbb{R} \, . \tag{1}$$

Furthermore, the random vector

$$\mathbf{X}(\omega) = \left[X_1(\omega), \ldots, X_i(\omega), \ldots, X_M(\omega)\right]^T \in \mathbb{R}^M \tag{2}$$

contains M random variables. For the sake of simplicity all components in $\mathbf{X}(\omega)$ are assumed to be stochastically independent throughout this paper. Therefore, the joint probability density function (PDF) of the random vector $\mathbf{X}(\omega)$ reads

$$f_{\mathbf{X}}(\mathbf{x}) = \prod_{i=1}^{M} f_{X_i}(x_i) \, , \tag{3}$$

where $f_{X_i}(x_i)$ is the marginal distribution of the random variable X_i. Furthermore, let $Z(\omega)$ be a stochastic quantity that depends on the vector $\mathbf{X}(\omega)$, such that $Z(\omega) = Z(\mathbf{X}(\omega))$.

The polynomial chaos expansion, originally introduced by [26] and subsequently extended by [28, 29], can be used to represent the random variable $Z(\mathbf{X}(\omega))$. Following [17], the PC approximation of $Z(\omega)$ is given by

$$Z(\mathbf{X}(\omega)) \approx Z^{pc}(\mathbf{X}(\omega)) = \sum_{\alpha=0}^{P} z_\alpha \Psi_\alpha(\mathbf{X}(\omega)) \, . \tag{4}$$

The coefficients z_α are deterministic, while the orthonormal basis polynomials $\Psi_\alpha(\mathbf{X}(\omega))$ depend on the random input vector $\mathbf{X}(\omega)$. In the present paper, the representation of a stochastic quantity according to Eq. (4) is referred to as stochastic discretization. Furthermore, the terms PCE, PC expansion, PC variable, and chaos expansion are used interchangeably to denote $Z^{pc}(\mathbf{X}(\omega))$.

The basis polynomials in Eq. (4) are orthonormal with respect to the joint probability density function $f_{\mathbf{X}}(\mathbf{x})$ in Eq. (3) and satisfy the condition

$$\mathbb{E}[\Psi_\alpha(\mathbf{X})\Psi_\beta(\mathbf{X})] = \int_{D_{\mathbf{X}}} \Psi_\alpha(\mathbf{x})\Psi_\beta(\mathbf{x}) f_{\mathbf{X}}(\mathbf{x}) \, \mathrm{d}\mathbf{x} = \delta_{\alpha\beta} \, . \tag{5}$$

Here, $\mathbb{E}[\bullet]$ denotes the mathematical expectation operator and $\delta_{\alpha\beta}$ the Kronecker delta.

Each polynomial $\Psi_\alpha(\mathbf{X}(\omega))$ in Eq. (4) is characterized by a corresponding multi-index

$$\boldsymbol{m}_\alpha = (m_1, \ldots, m_i, \ldots, m_M) \, , \quad m_i \in \mathbb{N} \, , \tag{6}$$

where m_i denotes the individual polynomial degree in the i-th input dimension. Based on the maximum polynomial degree p, the q-norm q, and the number of input variables M, the hyperbolic index set $\mathscr{A}_q^{M,p}$ containing $\bar{P} = P + 1$ multi-indices is given by

$$\begin{aligned} \mathscr{A}_q^{M,p} &= \left\{ \boldsymbol{m} \in \mathbb{N}^M : \ ||\boldsymbol{m}||_q \leq p \right\} \, , \\ ||\boldsymbol{m}||_q &= \left(\sum_{i=1}^{M} m_i^q \right)^{1/q} \, , \quad q \in (0, \, 1] \, . \end{aligned} \tag{7}$$

The hyperbolic truncation scheme in Eq. (7) was originally introduced by [5].

Due to the intrusive nature of the spectral stochastic FEM, the governing equations of the problem at hand have to be modified. Therefore, arithmetic operations, such as multiplication, division etc., have to be consistently reformulated in terms of PC variables, see Eq. (4). A detailed description and discussion of these issues can be found, e.g., in [7, 13].

In this paper, varying material properties are described by Gaussian random variables, and the spatial variability of structural parameters is modeled using Gaussian random fields. Since a normal distribution is defined for all real numbers, it is unbounded and can theoretically result in non-physical values for material parameters. In this paper, a coefficient of variation of 10 % is used to ensure a negligible probability of negative values.

Due to the Gaussian statistics of random variables and random fields, Hermite polynomials are applied for the stochastic discretization with the PCE. Details on the PC expansion of a random field are provided in Appendix A.

3 General framework for nonlinear SSFEM problems

This section provides a brief summary of the governing equations for geometrically nonlinear problems within the framework of the SSFEM. Furthermore, the main steps of the two-step discretization scheme are presented. A detailed derivation of a geometrically nonlinear stochastic shell element is provided in [13]. For the sake of simplicity the

equations in this section refer to a three-dimensional continuum.

3.1 Variational formulation

The basis for the development of spectral stochastic FE formulations is given by the stochastic variational principle

$$\delta\pi(\omega) = \delta\pi_i(\omega) - \delta\pi_a(\omega) = 0 \,, \tag{8}$$

where the dependence on ω indicates the random nature of the virtual internal work $\delta\pi_i(\omega)$ and virtual external work $\delta\pi_a(\omega)$. The weak form reads

$$\mathbb{E}[\delta\pi(\omega)] = \mathbb{E}[\delta\pi_i(\omega)] - \mathbb{E}[\delta\pi_a(\omega)] = 0 \,. \tag{9}$$

The expression in Eq. (9) enforces the expression in Eq. (8) in the stochastic dimension solely in the mean sense [10].

The virtual work of internal and external forces for a continuum with the volume Ω_0 and the Neumann boundary $\partial\Omega_0^\sigma$ is given by

$$\begin{aligned}\mathbb{E}[\delta\pi(\omega)] = \mathbb{E}\Big[\int_{\Omega_0} \delta\mathbf{E}^T(\omega)\mathbf{S}(\omega)\,\mathrm{d}V\Big] \\ - \mathbb{E}\Big[\int_{\Omega_0} \delta\mathbf{u}^T(\omega)\varrho\bar{\mathbf{b}}(\omega)\,\mathrm{d}V + \int_{\partial\Omega_0^\sigma} \delta\mathbf{u}^T(\omega)\bar{\mathbf{t}}(\omega)\,\mathrm{d}A\Big] \,.\end{aligned} \tag{10}$$

Here, $\mathbf{E}(\omega)$ and $\mathbf{S}(\omega)$ are the stochastic Green-Lagrangian strain tensor and the 2^{nd}-Piola-Kirchhoff stress tensor, respectively, in their Voigt notation. The primary field variable is the stochastic displacement field, denoted by $\mathbf{u}(\omega)$. Furthermore, $\delta(\bullet)$ represents the corresponding variation of a quantity of interest $(\bullet)$. The virtual external load includes body forces $\varrho\bar{\mathbf{b}}(\omega)$ acting on the three-dimensional continuum and surface tractions $\bar{\mathbf{t}}(\omega)$.

In order to solve the nonlinear equation in Eq. (10) within a Newton iteration scheme, the linearization is required

$$\mathrm{L}\big[\mathbb{E}[\delta\pi(\omega)]\big] = \mathbb{E}[\delta\pi(\omega)] + \mathbb{E}[\Delta\delta\pi(\omega)] = 0 \,. \tag{11}$$

For conservative loads, the linear increment of the virtual forces in Eq. (11) is given by

$$\mathbb{E}[\Delta\delta\pi(\omega)] = \mathbb{E}\Big[\int_{\Omega_0} \delta\mathbf{E}^T(\omega)\Delta\mathbf{S}(\omega) + \Delta\delta\mathbf{E}^T(\omega)\mathbf{S}(\omega)\,\mathrm{d}V\Big] \,. \tag{12}$$

For a purely displacement-based variational principle, it follows that

$$\delta\pi(\omega) = \delta\pi(\mathbf{u}(\mathbf{X},\omega)) \,, \tag{13}$$

where ω and $\mathbf{X}$ denote the random and spatial dependence of the displacement field $\mathbf{u}(\mathbf{X},\omega)$, respectively.

A two-stage discretization scheme is used to approximate the field variable $\mathbf{u}(\mathbf{X},\omega)$. The stochastic discretization is carried out in the first step. By means of the PCE, the approximation reads

$$\mathbf{u}(\mathbf{X},\omega) = \sum_{\alpha=0}^{P} \Psi_\alpha(\omega)\mathbf{u}_\alpha(\mathbf{X}) \,, \tag{14}$$

where $\mathbf{u}_\alpha(\mathbf{X})$ are the spatially varying PC coefficients of the displacement field. In a second step, these coefficients are discretized in the spatial domain using the FEM

$$\mathbf{u}_\alpha(\mathbf{X}) = \sum_{I=1}^{nel} N_I(\mathbf{X})\mathbf{v}_{I\alpha} \,, \quad \forall\,\alpha \in \{0,\ldots,P\} \,, \tag{15}$$

where $N_I(\mathbf{X})$ are standard shape functions and nel denotes the number of nodes per element e. The vector $\mathbf{v}_{I\alpha}$ contains the nodal displacements associated with node I and the basis polynomial $\Psi_\alpha(\omega)$.

Taking into account both discretization schemes in Eqs. (14) and (15), the complete approximation of the stochastic field variable $\mathbf{u}(\mathbf{X},\omega)$ is formulated as

$$\mathbf{u}(\mathbf{X},\omega) = \sum_{\alpha=0}^{P}\sum_{I=1}^{nel} \Psi_\alpha(\omega)N_I(\mathbf{X})\mathbf{v}_{I\alpha} \,. \tag{16}$$

A similar expression to that in Eq. (16) is also presented in [2]. The two-stage discretization scheme becomes apparent from the formulation in Eq. (16). The following two sections outline the principal steps involved in the SSFEM.

3.2 Stochastic discretization using the PCE

The stochastic discretization of the linearized weak form in Eq. (11) is given by

$$\mathbb{E}[\delta\pi(\omega)] + \mathbb{E}[\Delta\delta\pi(\omega)] \approx \mathbb{E}[\delta\pi^{pc}] + \mathbb{E}[\Delta\delta\pi^{pc}] \,, \tag{17}$$

where $(\bullet)^{pc}$ denotes the approximation with the PCE. Depending on the PC coefficients, the virtual work of the internal and external forces reads

$$\begin{aligned}\mathbb{E}[\delta\pi^{pc}] &= \mathbb{E}[\Psi_\alpha\Psi_\beta]\int_{\Omega_0} \delta\mathbf{E}_\alpha^T\mathbf{S}_\beta\,\mathrm{d}V \\ &\quad - \mathbb{E}[\Psi_\alpha\Psi_\beta]\Big[\int_{\Omega_0} \delta\mathbf{u}_\alpha^T\varrho\bar{\mathbf{b}}_\beta\,\mathrm{d}V + \int_{\partial\Omega_0^\sigma} \delta\mathbf{u}_\alpha^T\bar{\mathbf{t}}_\beta\,\mathrm{d}A\Big] \\ &= \int_{\Omega_0} \delta\mathbf{E}_\alpha^T\mathbf{S}_\alpha - \delta\mathbf{u}_\alpha^T\varrho\bar{\mathbf{b}}_\alpha\,\mathrm{d}V - \int_{\partial\Omega_0^\sigma} \delta\mathbf{u}_\alpha^T\bar{\mathbf{t}}_\alpha\,\mathrm{d}A \,.\end{aligned} \tag{18}$$

Due to the orthonormality condition in Eq. (5), $\mathbb{E}[\Psi_\alpha \Psi_\beta] = \delta_{\alpha\beta}$ holds. For the sake of simplicity, the summation signs are omitted. According to the Einstein summation convention, summation is performed over indices that appear twice, where all Greek indices range over the set $\{0, \dots, P\}$.

The linear increment of the virtual forces is formulated in the same manner

$$\begin{aligned}\mathbb{E}[\Delta\delta\pi^{pc}] &= \mathbb{E}[\Psi_\alpha\Psi_\beta]\int_{\Omega_0} \delta\mathbf{E}_\alpha^T \Delta\mathbf{S}_\beta + \Delta\delta\mathbf{E}_\alpha^T \mathbf{S}_\beta \,\mathrm{d}V \\ &= \int_{\Omega_0} \delta\mathbf{E}_\alpha^T \Delta\mathbf{S}_\alpha + \Delta\delta\mathbf{E}_\alpha^T \mathbf{S}_\alpha \,\mathrm{d}V \\ &= \int_{\Omega_0} \delta\mathbf{E}_\alpha^T \mathbf{C}_{\alpha\beta}\Delta\mathbf{E}_\beta + \Delta\delta\mathbf{E}_\alpha^T \mathbf{S}_\alpha \,\mathrm{d}V\ .\end{aligned} \tag{19}$$

For a compact notation of Eqs. (18) and (19), all PC coefficients are summarized in the vectors as follows

$$\begin{aligned}\delta\mathbf{u} &:= \left[\delta\mathbf{u}_0^T, \dots, \delta\mathbf{u}_P^T\right]^T, \qquad \delta\mathbf{E} := \left[\delta\mathbf{E}_0^T, \dots, \delta\mathbf{E}_P^T\right]^T, \\ \Delta\mathbf{E} &:= \left[\Delta\mathbf{E}_0^T, \dots, \mathbf{E}_P^T\right]^T, \qquad \mathbf{S} := \left[\mathbf{S}_0^T, \dots, \mathbf{S}_P^T\right]^T, \\ \Delta\delta\mathbf{E} &:= \left[\Delta\delta\mathbf{E}_0^T, \dots, \Delta\delta\mathbf{E}_P^T\right]^T, \ \bar{\mathbf{b}} := \left[\bar{\mathbf{b}}_0^T, \dots, \bar{\mathbf{b}}_P^T\right]^T, \\ \bar{\mathbf{t}} &:= \left[\bar{\mathbf{t}}_0^T, \dots, \bar{\mathbf{t}}_P^T\right]^T\ .\end{aligned} \tag{20}$$

Furthermore, the augmented material matrix is defined as

$$\mathbf{C} := \begin{bmatrix} \mathbf{C}_{00} & \dots & \mathbf{C}_{0P} \\ \vdots & \mathbf{C}_{\alpha\beta} & \vdots \\ \mathbf{C}_{P0} & \dots & \mathbf{C}_{PP} \end{bmatrix}\ . \tag{21}$$

For a linear elastic material behavior, $\mathbf{C}_{\alpha\beta} = D_{\alpha\beta\gamma}\mathbf{C}_\gamma$, where $\mathbf{C}_\gamma$ denotes the coefficients of the PC expansion of the stochastic material matrix $\mathbf{C}(\omega)$. An illustrative example of the PC expansion of a stochastic material matrix is given in Appendix E of [13].

Taking into account Eqs. (20) and (21), the semidiscrete linearized weak form reads

$$\begin{aligned}\mathrm{L}\left[\mathbb{E}[\delta\pi^{pc}]\right] = &\int_{\Omega_0} \delta\mathbf{E}^T\mathbf{S} - \delta\mathbf{u}^T\varrho\bar{\mathbf{b}}\,\mathrm{d}V - \int_{\partial\Omega_0^\sigma} \delta\mathbf{u}^T\bar{\mathbf{t}}\,\mathrm{d}A \\ &+ \int_{\Omega_0} \delta\mathbf{E}^T\mathbf{C}\Delta\mathbf{E} + \Delta\delta\mathbf{E}^T\mathbf{S}\,\mathrm{d}V\ .\end{aligned} \tag{22}$$

At this point, it should be noted that Eq. (22) is discrete in the stochastic dimension but is still continuous in the spatial domain.

3.3 Spatial discretization using the FEM

The general finite element discretization of the deterministic reference configuration Ω_0 in *numel* elements is given by

$$\Omega_0 \approx \Omega^h = \bigcup_{e=1}^{numel} \Omega_e\ , \tag{23}$$

where Ω_e denotes the domain of a single element e and the superscript $(\bullet)^h$ indicates the FE approximation. Taking into account the FE discretization, the discrete form of Eq. (22) is written as

$$\begin{aligned}\mathrm{L}\left[\mathbb{E}[\delta\pi^{pc}]\right] &\approx \mathrm{L}\left[\mathbb{E}[\delta\pi^{pc,h}]\right] \\ &= \mathbb{E}[\delta\pi^{pc,h}] + \mathbb{E}[\Delta\delta\pi^{pc,h}] \\ &= \bigcup_{e=1}^{numel} \left(\mathbb{E}[\delta\pi^{pc,h,e}] + \mathbb{E}[\Delta\delta\pi^{pc,h,e}]\right) = 0\ .\end{aligned} \tag{24}$$

The complete discretization of the weak form in Eq. (18) at the element level reads

$$\begin{aligned}\mathbb{E}[\delta\pi^{pc,h,e}] &= \mathbb{E}[\delta\pi_i^{pc,h,e}] - \mathbb{E}[\delta\pi_a^{pc,h,e}] \\ &= \sum_I \delta\mathbf{v}_I^T\Big(\int_{\Omega^e} \mathbf{B}_I^T\mathbf{S}\,\mathrm{d}V - \mathbf{p}_I\Big) \\ &= \sum_I \delta\mathbf{v}_I^T(\mathbf{f}_I - \mathbf{p}_I) = \sum_I \delta\mathbf{v}_I^T\mathbf{g}_I = \delta\mathbf{v}^{eT}\mathbf{g}^e\ ,\end{aligned} \tag{25}$$

where $\mathbf{g}^e$ is the element residual vector. Similar to this, the complete approximation of the linear increment in Eq. (19) yields

$$\begin{aligned}\mathbb{E}[\Delta\delta\pi^{pc,h,e}] &= \sum_I\sum_K \delta\mathbf{v}_I^T\left(\int_{\Omega^e} \mathbf{B}_I^T\mathbf{C}\,\mathbf{B}_K + \mathbf{G}_{IK}\,\mathrm{d}V\right)\Delta\mathbf{v}_K \\ &= \sum_I\sum_K \delta\mathbf{v}_I^T\,\mathbf{k}_{TIK}\,\Delta\mathbf{v}_K = \delta\mathbf{v}^{eT}\,\mathbf{k}_T^e\,\Delta\mathbf{v}^e\ .\end{aligned} \tag{26}$$

Here, $\mathbf{k}_T^e$ denotes the tangent stiffness matrix for an element e. Furthermore, $\mathbf{B}_I$ and $\mathbf{G}_{IK}$ represent the so-called B-matrix and the integrand of the geometric stiffness matrix, respectively. The entries of these two quantities depend on the respective element formulation, see e.g. [12, 13].

Assembling all arrays at the element level leads to the global vectors and matrices

$$\delta\mathbf{v} = \bigcup_{e=1}^{numel} \delta\mathbf{v}^e \,, \quad \Delta\mathbf{v} = \bigcup_{e=1}^{numel} \Delta\mathbf{v}^e \,, \quad \mathbf{G} = \bigcup_{e=1}^{numel} \mathbf{g}^e \,, \quad \mathbf{K}_T = \bigcup_{e=1}^{numel} \mathbf{k}_T^e \,. \tag{27}$$

Finally, the discrete form of Eq. (11) reads

$$\mathrm{L}\big[\mathbb{E}[\delta\pi^{pc,h}]\big] = \delta\mathbf{v}^T\big(\mathbf{K}_T\,\Delta\mathbf{v} + \mathbf{G}\big) = 0 \,. \tag{28}$$

Since the virtual displacements $\delta\mathbf{v}$ are arbitrary but non-zero, Eq. (28) leads to the linear system of equations

$$\mathbf{K}_T\,\Delta\mathbf{v} = -\mathbf{G} \,, \tag{29}$$

which has to be solved within an incremental-iterative solution algorithm.

4 Standard solution algorithms for spectral stochastic finite element problems

The two-step discretization procedure of the weak form in Eq. (9) leads to a system of nonlinear algebraic equations

$$\mathbf{G}(\mathbf{v}) = \mathbf{F}(\mathbf{v}) - \mathbf{P} = \mathbf{0} \,. \tag{30}$$

$\mathbf{G}(\mathbf{v})$ is the global residual vector, which denotes the difference between the vector of internal forces $\mathbf{F}(\mathbf{v})$ and the vector of external forces $\mathbf{P}$. With the introduction of a so-called load factor λ, Eq. (30) is rewritten

$$\mathbf{G}(\mathbf{v},\lambda) = \mathbf{F}(\mathbf{v}) - \lambda\mathbf{P} = \mathbf{0} \,, \quad \mathbf{G},\ \mathbf{F},\ \mathbf{P} \in \mathbb{R}^{ndof\cdot\bar{P}}, \tag{31}$$

where $ndof$ is the total number of deterministic degrees of freedom. In case of a geometrically nonlinear formulation, Eq. (31) is nonlinear in the displacement variables sought, which are summarized in the vector $\mathbf{v} \in \mathbb{R}^{ndof\cdot\bar{P}}$. For visibility of the individual PC coefficients of the global vectors, Eq. (31) is expressed as

$$\begin{bmatrix} \mathbf{G}_0 \\ \vdots \\ \mathbf{G}_\alpha \\ \vdots \\ \mathbf{G}_P \end{bmatrix} = \begin{bmatrix} \mathbf{F}_0 \\ \vdots \\ \mathbf{F}_\alpha \\ \vdots \\ \mathbf{F}_P \end{bmatrix} - \lambda \begin{bmatrix} \mathbf{P}_0 \\ \vdots \\ \mathbf{P}_\alpha \\ \vdots \\ \mathbf{P}_P \end{bmatrix} \,, \quad \mathbf{G}_\alpha,\ \mathbf{F}_\alpha,\ \mathbf{P}_\alpha \in \mathbb{R}^{ndof} \,. \tag{32}$$

For the special case of deterministic external loads, it holds $\mathbf{P}_\alpha = \mathbf{0},\ \forall\alpha > 0$.

To solve the algebraic nonlinear system of equations in Eq. (31) within a Newton iteration scheme, the discrete linearization

$$\mathbf{K}_T\,\Delta\mathbf{v} = -\mathbf{G} \,, \quad \mathbf{K}_T \in \mathbb{R}^{(ndof\cdot\bar{P})\times(ndof\cdot\bar{P})},\ \Delta\mathbf{v} \in \mathbb{R}^{ndof\cdot\bar{P}} \tag{33}$$

is required. An equivalent formulation in terms of the individual PC coefficients reads

$$\begin{bmatrix} \mathbf{K}_{T00} & \cdots & \mathbf{K}_{T0\beta} & \cdots & \mathbf{K}_{T0P} \\ \vdots & \ddots & \vdots & \ddots & \vdots \\ \mathbf{K}_{T\alpha0} & \cdots & \mathbf{K}_{T\alpha\beta} & \cdots & \mathbf{K}_{T\alpha P} \\ \vdots & \ddots & \vdots & \ddots & \vdots \\ \mathbf{K}_{TP0} & \cdots & \mathbf{K}_{TP\beta} & \cdots & \mathbf{K}_{TPP} \end{bmatrix} \begin{bmatrix} \Delta\mathbf{v}_0 \\ \vdots \\ \Delta\mathbf{v}_\beta \\ \vdots \\ \Delta\mathbf{v}_P \end{bmatrix} = - \begin{bmatrix} \mathbf{G}_0 \\ \vdots \\ \mathbf{G}_\alpha \\ \vdots \\ \mathbf{G}_P \end{bmatrix} \,. \tag{34}$$

For the individual submatrices, $\mathbf{K}_{T\alpha\beta} \in \mathbb{R}^{ndof\times ndof}$ holds.

Based on Eq. (31) and its corresponding discrete linearization in Eq. (33), two incremental-iterative solution algorithms are described in the following. Sections 4.1 and 4.2 outline the load control and the single displacement control for spectral stochastic finite element problems. The two algorithms described in the present paper were also discussed in [14] in connection with the SSFEM.

4.1 Load control

Within the load control, the external load vector $\mathbf{P}$ is controlled with the load factor λ, see Eq. (31). To exploit the local quadratic convergence behavior of the Newton method near an equilibrium point, the external force is not applied in a single step but is increased incrementally. For the sake of completeness, the main steps of the iterative solution algorithm are briefly outlined.

Starting from a known equilibrium point $\mathbf{G}(\mathbf{v}^{(n)},\lambda^{(n)}) = \mathbf{0}$, the external load is increased with $\lambda^{(n+1)} = \lambda^{(n)} + \Delta\lambda$. The superscript $(\bullet)^{(n)}$ specifies the corresponding load state. The displacement vector $\mathbf{v}^{(n+1)}$ associated with the load value $\lambda^{(n+1)}$ is determined iteratively. At the beginning of the Newton iteration, $i = 0$ holds. The displacement increment $\Delta\mathbf{v}_i^{(n)}$ in the n-th load step and the i-th Newton iteration is determined by solving the discrete linearization

$$\mathbf{K}_T(\mathbf{v}_i^{(n)})\Delta\mathbf{v}_i^{(n)} = -\mathbf{G}(\mathbf{v}_i^{(n)},\lambda^{(n+1)}) \,. \tag{35}$$

Subsequently, the displacements are updated with

$$\mathbf{v}_{i+1}^{(n)} = \mathbf{v}_i^{(n)} + \Delta\mathbf{v}_i^{(n)} \,. \tag{36}$$

The norm of the residual vector $||\mathbf{G}||$ is used as the convergence criterion for the Newton iteration. If this quantity is

smaller than a prescribed tolerance, the corresponding equilibrium point is reached.

A schematic flowchart of the load control in a finite element program is shown in Algorithm 1.

Algorithm 1 Load control

$\lambda^{(1)} = 0,\ \mathbf{v}_0^{(1)} = \mathbf{0}$ ▷ Initialization
for $n = 1, \ldots, N$ **do** ▷ Load loop
  $\lambda^{(n+1)} = \lambda^{(n)} + \Delta\lambda$ ▷ Increase load factor
  $i = 0$
  while $||\mathbf{G}|| > TOL$ **do** ▷ NEWTON loop
    for $e = 1, \ldots, numel$ **do** ▷ Element loop
      $\mathbf{g}^e$ and $\mathbf{k}_T^e$ ▷ Element residual and tangent
      $\mathbf{K}_T \leftarrow \mathbf{K}_T + \bigcup_e \mathbf{k}_T^e,\ \mathbf{G} \leftarrow \mathbf{G} + \bigcup_e \mathbf{g}^e$ ▷ Assembly
    end for
    $\mathbf{K}_T \Delta\mathbf{v}_i^{(n)} = -\mathbf{G}$ ▷ Displacement increment
    $\mathbf{v}_{i+1}^{(n)} = \mathbf{v}_i^{(n)} + \Delta\mathbf{v}_i^{(n)}$ ▷ Update displacements
    $i \leftarrow i + 1$
  end while
  $\mathbf{v}_i^{(n+1)} = \mathbf{v}_i^{(n)}$
end for

Illustrative example

As an illustrative example of the described load control, a simply supported beam under a constant line load is considered, see Fig. 1. The beam has a rectangular cross-section and the shear correction factor is $\kappa = 5/6$.

The Young's modulus is modeled as normal distributed random variable

$$E(\omega) \sim \mathcal{N}(1000, 100)\,\mathrm{kN/cm^2}\,. \tag{37}$$

The shear modulus is assumed to be fully correlated with the Young's modulus $G(\omega) = E(\omega)/2$. As a consequence of the stochastic material properties, the resulting deformations of the structure are random quantities.

The calculation is carried out using a two-dimensional geometrically exact beam formulation, see e.g. [16, 24, 27],

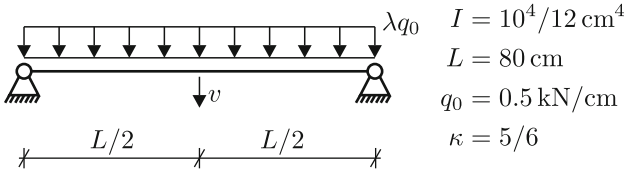

Fig. 1 Simply supported beam under distributed line load: system and geometry

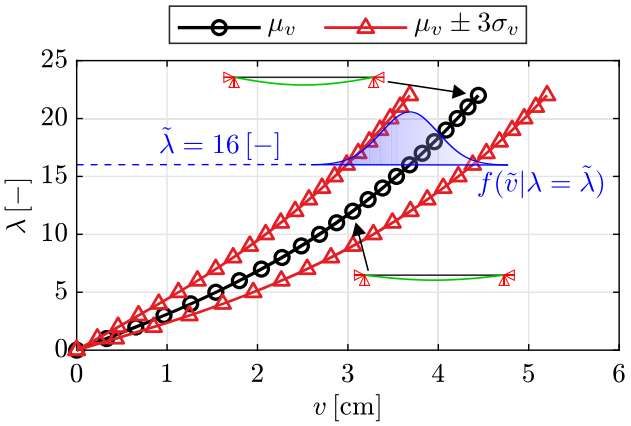

Fig. 2 Deterministic load factor λ versus the stochastic displacement v and a qualitative PDF of the displacement $\tilde{v}$ at the load level $\tilde{\lambda} = 16$

which has been consistently extended to the stochastic framework of the SSFEM. The whole structure is discretized with 20 elements. Furthermore, a quadratic polynomial basis with $p = 2$ is used for the stochastic discretization. In the simulation, the deterministic load q_0 is increased by the load factor λ. Here, 22 load steps with $\Delta\lambda = 1$ are used.

Figure 2 depicts the deterministic load factor λ versus the mean value of the center displacement v.

In order to illustrate the variation of the random center displacement v, the mean value μ_v plus minus three times the standard deviation σ_v is shown. For the load level $\tilde{\lambda} = 16$, the corresponding random displacement is denoted by $\tilde{v}$. In addition, a qualitative probability density function (PDF) $f(\tilde{v}|\lambda = \tilde{\lambda})$ of the displacement at the load level $\tilde{\lambda} = 16$ is depicted in Fig. 2.

4.2 Single displacement control

Within this solution algorithm, a user-defined displacement quantity v^{c} respectively the associated polynomial chaos coefficients $\{v_\alpha^{\mathrm{c}}\}_{\alpha=0}^{P}$ are controlled. In order to take advantage of the local quadratic convergence behavior of the Newton method, the specified displacement is not applied in one step, but is increased incrementally.

In a first step, the global displacement vector $\mathbf{v}$ respectively the vector of increments $\Delta\mathbf{v}$ is divided into free (f) and constrained (c) quantities

$$\Delta\mathbf{v} = \begin{bmatrix} \Delta\mathbf{v}^{\mathrm{f}} \\ \Delta\mathbf{v}^{\mathrm{c}} \end{bmatrix}\,. \tag{38}$$

A more precise representation in terms of the PC coefficients is given by

$$\Delta\mathbf{v}^{\mathrm{f}} = \begin{bmatrix} \Delta\mathbf{v}_0^{\mathrm{f}} \\ \vdots \\ \Delta\mathbf{v}_\alpha^{\mathrm{f}} \\ \vdots \\ \Delta\mathbf{v}_P^{\mathrm{f}} \end{bmatrix} \in \mathbb{R}^{(ndof-1)\bar{P}} , \quad \Delta\mathbf{v}^{\mathrm{c}} = \begin{bmatrix} \Delta v_0^{\mathrm{c}} \\ \vdots \\ \Delta v_\alpha^{\mathrm{c}} \\ \vdots \\ \Delta v_P^{\mathrm{c}} \end{bmatrix} \in \mathbb{R}^{\bar{P}} . \tag{39}$$

All chaos coefficients of the prescribed displacement quantity are summarized in the vector $\Delta\mathbf{v}^{\mathrm{c}}$. Within the solution algorithm, this degree of freedom is deterministic. Accordingly, the individual components of the vector $\Delta\mathbf{v}^{\mathrm{c}}$ in Eq. (39) read

$$\left[\Delta v_0^{\mathrm{c}}, \ldots, \Delta v_\alpha^{\mathrm{c}}, \ldots, \Delta v_P^{\mathrm{c}}\right]^T = \left[\Delta v^{\mathrm{c}}, \ldots, 0, \ldots, 0\right]^T . \tag{40}$$

The constrained displacement quantity $\mathbf{v}^{\mathrm{c}}$ respectively the corresponding PC coefficients are controlled during this solution algorithm.

Based on the split in Eq. (38), the discrete linearization in Eq. (33) is partitioned in the same manner

$$\begin{bmatrix} \mathbf{K}_T^{\mathrm{ff}} & \mathbf{K}_T^{\mathrm{fc}} \\ \mathbf{K}_T^{\mathrm{cf}} & \mathbf{K}_T^{\mathrm{cc}} \end{bmatrix} \begin{bmatrix} \Delta\mathbf{v}^{\mathrm{f}} \\ \Delta\mathbf{v}^{\mathrm{c}} \end{bmatrix} = - \begin{bmatrix} \mathbf{G}^{\mathrm{f}} \\ \mathbf{G}^{\mathrm{c}} \end{bmatrix} . \tag{41}$$

The submatrices in Eq. (41) have the following dimensions

$$\begin{aligned} &\mathbf{K}_T^{\mathrm{ff}} \in \mathbb{R}^{((ndof-1)\bar{P})\times((ndof-1)\bar{P})} , \quad \mathbf{K}_T^{\mathrm{fc}} \in \mathbb{R}^{((ndof-1)\bar{P})\times\bar{P}} , \\ &\mathbf{K}_T^{\mathrm{cf}} \in \mathbb{R}^{\bar{P}\times((ndof-1)\bar{P})} \quad \text{and} \quad \mathbf{K}_T^{\mathrm{cc}} \in \mathbb{R}^{\bar{P}\times\bar{P}} . \end{aligned} \tag{42}$$

The symmetry of the global stiffness matrix $\mathbf{K}_T$ leads to the fact that the relation $\mathbf{K}_T^{\mathrm{cf}} = (\mathbf{K}_T^{\mathrm{fc}})^T$ holds to the two subdiagonal matrices. In terms of the individual components, the reordering of the global tangent stiffness matrix is given by

$$\mathbf{K}_T = \begin{bmatrix} \begin{bmatrix} \mathbf{K}_{T00}^{\mathrm{ff}} & \cdots & \mathbf{K}_{T0P}^{\mathrm{ff}} \\ \vdots & \mathbf{K}_{T\alpha\beta}^{\mathrm{ff}} & \vdots \\ \mathbf{K}_{TP0}^{\mathrm{ff}} & \cdots & \mathbf{K}_{TPP}^{\mathrm{ff}} \end{bmatrix} & \begin{bmatrix} \mathbf{K}_{T0}^{\mathrm{fc}} \cdots \mathbf{K}_{TP}^{\mathrm{fc}} \end{bmatrix} \\ \begin{bmatrix} \mathbf{K}_{T0}^{\mathrm{fc}^T} \\ \vdots \\ \mathbf{K}_{TP}^{\mathrm{fc}^T} \end{bmatrix} & \begin{bmatrix} K_{T00}^{\mathrm{cc}} & \cdots & K_{T0P}^{\mathrm{cc}} \\ \vdots & K_{T\alpha\beta}^{\mathrm{cc}} & \vdots \\ K_{TP0}^{\mathrm{cc}} & \cdots & K_{TPP}^{\mathrm{cc}} \end{bmatrix} \end{bmatrix} . \tag{43}$$

Within the single displacement control, the external load is zero, leading to $\mathbf{P} = \mathbf{0}$. Due to this reason, the right hand-side of Eq. (41) simplifies to

$$\begin{bmatrix} \mathbf{G}^{\mathrm{f}} \\ \mathbf{G}^{\mathrm{c}} \end{bmatrix} = \begin{bmatrix} \mathbf{F}^{\mathrm{f}} - \mathbf{P}^{\mathrm{f}} \\ \mathbf{F}^{\mathrm{c}} - \mathbf{P}^{\mathrm{c}} - \mathbf{R}^{\mathrm{c}} \end{bmatrix} = \begin{bmatrix} \mathbf{F}^{\mathrm{f}} \\ \mathbf{F}^{\mathrm{c}} - \mathbf{R}^{\mathrm{c}} \end{bmatrix} , \tag{44}$$

where $\mathbf{R}^{\mathrm{c}}$ summarizes the $\bar{P}$ PC coefficients of the reaction force resulting from the prescribed displacement $\Delta\mathbf{v}^{\mathrm{c}}$

$$\mathbf{R}^{\mathrm{c}} = [R_0^{\mathrm{c}}, \ldots, R_\alpha^{\mathrm{c}}, \ldots, R_P^{\mathrm{c}}]^T \in \mathbb{R}^{\bar{P}} . \tag{45}$$

This reaction force is equivalent to the external load that has to be applied to the structure to induce the displacement increment $\Delta\mathbf{v}^{\mathrm{c}}$ at the degree of freedom (c).

Considering the first line of Eq. (41), the prescribed displacement increment $\Delta\mathbf{v}^{\mathrm{c}}$ together with the corresponding stiffness matrix $\mathbf{K}_T^{\mathrm{fc}}$ results in an effective force vector. This quantity is therefore moved to the right hand-side, leading to a modified residual vector denoted by $\bar{\mathbf{G}}^{\mathrm{f}}$. The first line of Eq. (41) is rewritten as

$$\begin{aligned} &\mathbf{K}_T^{\mathrm{ff}}\Delta\mathbf{v}^{\mathrm{f}} + \mathbf{K}_T^{\mathrm{fc}}\Delta\mathbf{v}^{\mathrm{c}} = -\mathbf{G}^{\mathrm{f}} , \\ \Leftrightarrow\ &\mathbf{K}_T^{\mathrm{ff}}\Delta\mathbf{v}^{\mathrm{f}} = -\left(\mathbf{G}^{\mathrm{f}} + \mathbf{K}_T^{\mathrm{fc}}\Delta\mathbf{v}^{\mathrm{c}}\right) =: -\bar{\mathbf{G}}^{\mathrm{f}} . \end{aligned} \tag{46}$$

Based on Eq. (46), the free displacement increments $\Delta\mathbf{v}^{\mathrm{f}}$ are determined.

The second line of Eq. (41) is subsequently used to calculate the PC coefficients of the reaction force $\mathbf{R}^{\mathrm{c}}$ at the constrained displacement

$$\begin{aligned} &\mathbf{K}_T^{\mathrm{cf}}\Delta\mathbf{v}^{\mathrm{f}} + \mathbf{K}_T^{\mathrm{cc}}\Delta\mathbf{v}^{\mathrm{c}} = -\left(\mathbf{F}^{\mathrm{c}} - \mathbf{R}^{\mathrm{c}}\right) \\ \Leftrightarrow\ &\mathbf{R}^{\mathrm{c}} = \mathbf{K}_T^{\mathrm{cf}}\Delta\mathbf{v}^{\mathrm{f}} + \mathbf{K}_T^{\mathrm{cc}}\Delta\mathbf{v}^{\mathrm{c}} + \mathbf{F}^{\mathrm{c}} . \end{aligned} \tag{47}$$

A schematic flowchart of the single displacement control implemented in a finite element program is shown in Algorithm 2.

Illustrative example

As an illustrative example of the described single displacement control, the kinked beam under single load, shown in Fig. 3, is considered. The beam has a rectangular cross-section and the shear correction factor is $\kappa = 5/6$.

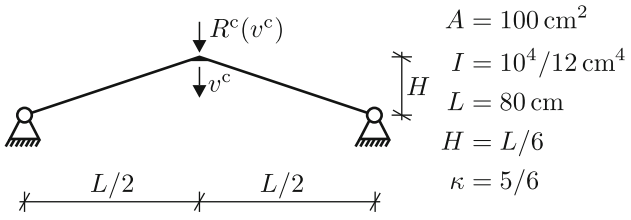

Fig. 3 Kinked beam under single load: system and geometry

Algorithm 2 Single displacement control

$\mathbf{v}_0^{(0)} = \mathbf{0}$ ▷ Initialization
for $n = 1, \ldots, N$ **do** ▷ Load loop
  $i = 0$
  $\mathbf{v}_i^{\mathrm{c},(n)} = \mathbf{v}_i^{\mathrm{c},(n-1)} + \Delta\mathbf{v}^{\mathrm{c}}$ ▷ Increase prescribed displacement
  while $||\mathbf{G}|| > TOL$ **do** ▷ NEWTON loop
    if $i > 0$ **then**
      $\Delta\mathbf{v}^{\mathrm{c}} = \mathbf{0}$
    end if
    for $e = 1, \ldots, numel$ **do** ▷ Element loop
      $\mathbf{g}^e$ and $\mathbf{k}_T^e$ ▷ Element residual and tangent
      $\mathbf{K}_T \leftarrow \mathbf{K}_T + \bigcup_e \mathbf{k}_T^e,\ \mathbf{G} \leftarrow \mathbf{G} + \bigcup_e \mathbf{g}^e$ ▷ Assembly
    end for
    $\bar{\mathbf{G}}^{\mathrm{f}} = \mathbf{G}^{\mathrm{f}} + \mathbf{K}_T^{\mathrm{fc}}\Delta\mathbf{v}^{\mathrm{c}}$ ▷ Modified residual
    $\mathbf{K}_T^{\mathrm{ff}}\Delta\mathbf{v}_i^{\mathrm{f},(n)} = -\bar{\mathbf{G}}^{\mathrm{f}}$ ▷ Displacement increment
    $\mathbf{R}^{\mathrm{c},(n)} = \mathbf{K}_T^{\mathrm{cf}}\Delta\mathbf{v}_i^{\mathrm{f},(n)} + \mathbf{K}_T^{\mathrm{cc}}\Delta\mathbf{v}^{\mathrm{c}} + \mathbf{F}^{\mathrm{c}}$ ▷ Reaction force
    $\mathbf{v}_{i+1}^{\mathrm{f},(n)} = \mathbf{v}_i^{\mathrm{f},(n)} + \Delta\mathbf{v}_i^{\mathrm{f},(n)}$ ▷ Update free displacements
    $i \leftarrow i + 1$
  end while
  $\mathbf{v}_i^{(n+1)} = \mathbf{v}_i^{(n)} = \begin{bmatrix} \mathbf{v}_i^{\mathrm{f},(n)} \\ \mathbf{v}_i^{\mathrm{c},(n)} \end{bmatrix}$
end for

The Young's modulus is modeled as normal distributed random variable

$$E(\omega) \sim \mathcal{N}(1000, 100)\,\mathrm{kN/cm^2}\,. \tag{48}$$

For the shear modulus, it applies $G(\omega) = E(\omega)/2$. The spatial and stochastic discretization are equivalent to the principle example in Sect. 4.1. Consequently, each beam of the structure is divided into 10 elements. The dimensions and material properties are chosen such that the entire structure reaches its limit point before any single beam fails. By prescribing the displacement v^{c}, the load is applied on the structure. Here, 22 load steps with $\Delta v^{\mathrm{c}} = 1\,\mathrm{cm}$ are used. At this point, it should be noted again, that the controlled displacement is deterministic.

Due to the random material properties of the structure, the reaction force $R^{\mathrm{c}}(v^{\mathrm{c}})$ and the remaining displacements of the structure are stochastic quantities. Figure 4 shows the mean value $\mu_{R^{\mathrm{c}}}$ of the stochastic reaction force versus the prescribed displacement v^{c}.

In order to illustrate the variation of the stochastic reaction force $R^{\mathrm{c}}(v^{\mathrm{c}})$, the mean value $\mu_{R^{\mathrm{c}}}$ plus minus three times the standard deviation $\sigma_{R^{\mathrm{c}}}$ is depicted. For a given value of the controlled displacement $\tilde{v}^{\mathrm{c}} = 6\,\mathrm{cm}$, the corresponding stochastic reaction force is denoted by $\tilde{R}^{\mathrm{c}}$. In addition, a qualitative probability density function $f(\tilde{R}^{\mathrm{c}}|v^{\mathrm{c}} = \tilde{v}^{\mathrm{c}})$ of the reaction force at the displacement level $\tilde{v}^{\mathrm{c}} = 6\,\mathrm{cm}$ is shown in Fig. 4.

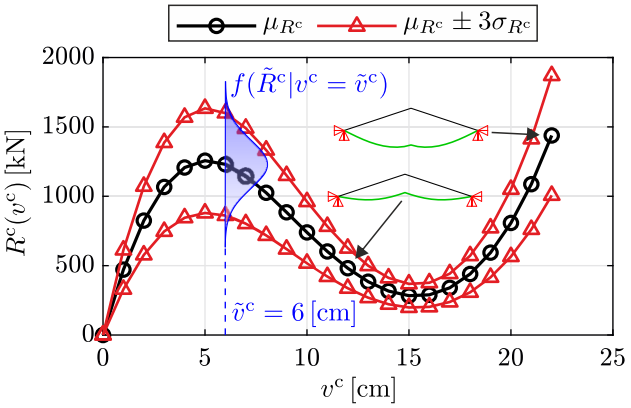

Fig. 4 Stochastic reaction force $R^{\mathrm{c}}(v^{\mathrm{c}})$ versus the deterministic displacement v^{c} and a qualitative PDF of the reaction force $\tilde{R}^{\mathrm{c}}$ at the load level $\tilde{v}^{\mathrm{c}} = 6\,\mathrm{cm}$

4.3 Concluding remarks

Based on the load control in Sect. 4.1 and the single displacement control in Sect. 4.2, it is evident that both solution algorithms can be used in an SSFEM calculation without any extensive modifications. The following list summarizes concluding remarks on both solution methods.

- The load control described in Sect. 4.1 allows the consideration of uncertainties in material and geometrical properties, as well as in the external load. In the case of a stochastic external load, this quantity is increased by the deterministic load factor λ, as shown in Eq. (32).
- An essential limitation of the single displacement control, described in Sect. 4.2, is that the only permissible external load is the reaction force corresponding to the prescribed displacement.
- In some cases, it is also possible to control several displacements on one edge, e.g., an axially loaded cylinder. This procedure then corresponds to a constant line load along that edge. The total reaction force is computed using the sum of all partial reaction forces at the prescribed displacements. It is important to note that this procedure is only valid if the prescribing of multiple displacements does not impose undesired kinematic constraints on the system.

Based on the points outlined above, it is evident that some problems, e.g., the snap-through of a kinked beam under dead load, cannot be investigated within the framework of the SSFEM using the solution algorithms described so far. The load control in Sect. 4.1 and the single displacement control in Sect. 4.2 do not allow the computation of the two numerical examples in Sects. 7.2 and 7.3.

Therefore, the following section presents a generalized displacement control that can be used for computations with

the SSFEM and overcomes the aforementioned limitations of existing solution algorithms.

5 Generalized displacement control for spectral stochastic finite element problems

5.1 Proposed algorithm

The original version of the solution algorithm further developed in the present paper can be found in e.g. [4, 25].

Within the proposed generalized displacement control, similar to the solution algorithm in Sect. 4.2, a user-defined displacement quantity is controlled. In contrast to the single displacement control, however, a load factor is computed for the external load instead of determining a reaction force.

Hence, the load factor λ in Eq. (31) is, in general, no longer a deterministic quantity. As well as the stochastic reaction force in Eq. (45), the stochastic load factor λ is now specified by its PC coefficients $\{\lambda_\alpha\}_{\alpha=0}^{P}$. Therefore, the global residual vector in Eq. (31) has to be reformulated. Up to now, the α-th coefficient of the global residual was $\mathbf{G}_\alpha = \mathbf{F}_\alpha - \lambda\mathbf{P}_\alpha$, see Eq. (32). The coefficient $\mathbf{G}_\alpha$ is now defined as

$$\mathbf{G}_\alpha = \mathbf{F}_\alpha - \bar{\mathbf{P}}_\alpha \,, \tag{49}$$

where the vector $\bar{\mathbf{P}}_\alpha$ contains the external load already scaled with the stochastic load factor. Since both, the load factor and the external load vector are in general stochastic quantities, the coefficients $\bar{\mathbf{P}}_\alpha$ are calculated with

$$\bar{\mathbf{P}}_\alpha = D_{\alpha\beta\gamma}\lambda_\beta\mathbf{P}_\gamma \,. \tag{50}$$

In the case of deterministic external loads, $\mathbf{P}_\gamma = \delta_{\gamma 0}\mathbf{P}_0$ holds. Therefore, Eq. (50) simplifies to

$$\bar{\mathbf{P}}_\alpha = D_{\alpha\beta\gamma}\lambda_\beta\delta_{\gamma 0}\mathbf{P}_0 = \delta_{\alpha\beta}\lambda_\beta\mathbf{P}_0 = \lambda_\alpha\mathbf{P}_0 \,. \tag{51}$$

Subsequently, the general form given in Eq. (50) is considered. For the following derivations, all PC coefficients of the stochastic load factor are gathered in the vector

$$\boldsymbol{\lambda} = [\lambda_0, \ldots, \lambda_\alpha, \ldots, \lambda_P]^T \in \mathbb{R}^{\bar{P}} \,. \tag{52}$$

From now on, the notation $\mathbf{G}(\mathbf{v}, \boldsymbol{\lambda})$ is used for the global residual vector.

The basic idea of the proposed solution algorithm is to extend Eq. (30) by a constraint $f(\bullet)$. To ensure that the displacement quantity v^{c} is equal to a prescribed value $\bar{v}^{\,\mathrm{c}}$ specified by the user, the constraint reads

$$f = v^{\mathrm{c}} - \bar{v}^{\,\mathrm{c}} \stackrel{!}{=} 0 \,. \tag{53}$$

In the context of the SSFEM, the displacement v^{c} is characterized by its $\bar{P}$ PC coefficients $\{v_\alpha^{\mathrm{c}}\}_{\alpha=0}^{P}$. For this reason, the constraint in Eq. (53) has to be formulated for all PC coefficients

$$f_\alpha = (v_\alpha^{\mathrm{c}} - \bar{v}_\alpha^{\mathrm{c}}) \stackrel{!}{=} 0 \,, \quad \forall\, \alpha \in \{0, \ldots, P\} \,. \tag{54}$$

Similar to the single displacement control in Sect. 4.2, the prescribed displacement is deterministic. Consequently, $\bar{v}_\alpha^{\mathrm{c}} = \delta_{\alpha 0}\bar{v}^{\,\mathrm{c}}$ holds. In vector notation, Eq. (54) reads

$$\mathbf{f}(\mathbf{v}) = \begin{bmatrix} f_0 \\ \vdots \\ f_\alpha \\ \vdots \\ f_P \end{bmatrix} = \begin{bmatrix} v_0^{\mathrm{c}} \\ \vdots \\ v_\alpha^{\mathrm{c}} \\ \vdots \\ v_P^{\mathrm{c}} \end{bmatrix} - \begin{bmatrix} \bar{v}^{\,\mathrm{c}} \\ \vdots \\ 0 \\ \vdots \\ 0 \end{bmatrix} = \mathbf{v}^{\mathrm{c}} - \bar{\mathbf{v}}^{\mathrm{c}} \,, \quad \mathbf{f}(\mathbf{v}) \in \mathbb{R}^{\bar{P}} \,, \tag{55}$$

where $\bar{v}^{\,\mathrm{c}}$ is specified by the user.

When the $\bar{P}$ equations in Eq. (55) are added to the global residual vector $\mathbf{G}(\mathbf{v}, \boldsymbol{\lambda})$, the extended system of nonlinear equations is given by

$$\bar{\mathbf{G}}(\mathbf{w}) := \begin{Bmatrix} \mathbf{G}(\mathbf{v}, \boldsymbol{\lambda}) \\ \mathbf{f}(\mathbf{v}) \end{Bmatrix} = \mathbf{0} \,, \quad \mathbf{w} = \begin{Bmatrix} \mathbf{v} \\ \boldsymbol{\lambda} \end{Bmatrix} \in \mathbb{R}^{(ndof+1)\bar{P}} \,, \tag{56}$$

where the generalized solution vector $\mathbf{w}$ contains all PC coefficients of the displacements and the load factor.

In order to solve the extended system of nonlinear equations in a Newton iteration scheme, the linearization of the augmented residual $\bar{\mathbf{G}}(\mathbf{w})$ has to be determined

$$\begin{aligned} \mathrm{L}[\bar{\mathbf{G}}(\mathbf{w})] &= \bar{\mathbf{G}}(\mathbf{w}) + \frac{\partial \bar{\mathbf{G}}}{\partial \mathbf{w}}\Delta\mathbf{w} \\ &= \bar{\mathbf{G}}(\mathbf{w}) + \underbrace{\frac{\partial \mathbf{G}}{\partial \mathbf{v}}\Delta\mathbf{v} + \frac{\partial \mathbf{f}}{\partial \mathbf{v}}\Delta\mathbf{v}}_{\frac{\partial \bar{\mathbf{G}}}{\partial \mathbf{v}}\Delta\mathbf{v}} + \underbrace{\frac{\partial \mathbf{G}}{\partial \boldsymbol{\lambda}}\Delta\boldsymbol{\lambda} + \frac{\partial \mathbf{f}}{\partial \boldsymbol{\lambda}}\Delta\boldsymbol{\lambda}}_{\frac{\partial \bar{\mathbf{G}}}{\partial \boldsymbol{\lambda}}\Delta\boldsymbol{\lambda}} \,. \end{aligned} \tag{57}$$

The partial derivative of the extended residual vector $\bar{\mathbf{G}}(\mathbf{w})$ with respect to the PC coefficients of the displacement vector reads

$$\frac{\partial \mathbf{G}_\alpha}{\partial \mathbf{v}_\mu} = \mathbf{K}_{T\alpha\mu} \in \mathbb{R}^{ndof \times ndof} \quad \text{and} \tag{58}$$

$$\frac{\partial f_\alpha}{\partial \mathbf{v}_\mu} = \frac{\partial (v_\alpha^c - \bar{v}_\alpha^c)}{\partial \mathbf{v}_\mu} = \delta_{\alpha\mu} \mathbf{f}_\mathrm{v}^T \quad \text{with} \quad \mathbf{f}_\mathrm{v}^T = [0, \ldots, \underbrace{1}_{\text{position (c)}}, \ldots, 0] \in \mathbb{R}^{ndof} \,. \tag{59}$$

The components of the vector $\mathbf{f}_\mathrm{v}^T$ derived in Eq. (59) are all zero except for the position (c), which has a value of one. The partial derivative of $\bar{\mathbf{G}}(\mathbf{w})$ with respect to the PC coefficients of the load factor is given by

$$\frac{\partial \mathbf{G}_\alpha}{\partial \lambda_\mu} = \frac{\partial \left(\mathbf{F}_\alpha - D_{\alpha\beta\gamma} \lambda_\beta \mathbf{P}_\gamma \right)}{\partial \lambda_\mu} = -D_{\alpha\mu\gamma} \mathbf{P}_\gamma = -\mathbf{P}_{\alpha\mu} \in \mathbb{R}^{ndof} \quad \text{and} \tag{60}$$

$$\frac{\partial f_\alpha}{\partial \lambda_\mu} = \delta_{\alpha\mu} 0 = 0 \,. \tag{61}$$

Since the constraint vector $\mathbf{f}(\mathbf{v})$ in Eq. (55) is not dependent on the PC coefficients of the load factor, the corresponding derivative in Eq. (61) is zero.

The individual submatrices $\mathbf{K}_{T\alpha\mu}$ in Eq. (58) are merged in the global stiffness matrix $\mathbf{K}_T$, see Eq. (34). In the same manner, the individual vectors $\delta_{\alpha\mu} \mathbf{f}_\mathrm{v}^T$ in Eq. (59) are arranged in the matrix

$$\widehat{\mathbf{f}}_\mathrm{v}^T = \begin{bmatrix} \mathbf{f}_\mathrm{v}^T & \cdots & \mathbf{0} & \cdots & \mathbf{0} \\ \vdots & \ddots & \vdots & \ddots & \vdots \\ \mathbf{0} & \cdots & \mathbf{f}_\mathrm{v}^T & \cdots & \mathbf{0} \\ \vdots & \ddots & \vdots & \ddots & \vdots \\ \mathbf{0} & \cdots & \mathbf{0} & \cdots & \mathbf{f}_\mathrm{v}^T \end{bmatrix} = \begin{bmatrix} - & \widehat{\mathbf{f}}_{\mathrm{v}0}^T & - \\ & \vdots & \\ - & \widehat{\mathbf{f}}_{\mathrm{v}\beta}^T & - \\ & \vdots & \\ - & \widehat{\mathbf{f}}_{\mathrm{v}P}^T & - \end{bmatrix}, \widehat{\mathbf{f}}_{\mathrm{v}\beta}^T \in \mathbb{R}^{1 \times (ndof \cdot \bar{P})} \,. \tag{62}$$

Here, $\widehat{\mathbf{f}}_{\mathrm{v}\beta}^T$ corresponds to the $(\beta + 1)$-th row of the matrix $\widehat{\mathbf{f}}_\mathrm{v}^T \in \mathbb{R}^{\bar{P} \times (ndof \cdot \bar{P})}$. Due to the Kronecker delta, $\widehat{\mathbf{f}}_\mathrm{v}^T$ equals a block diagonal matrix.

The matrix $\widehat{\mathbf{P}} \in \mathbb{R}^{(ndof \cdot \bar{P}) \times \bar{P}}$ contains the vectors $\mathbf{P}_{\alpha\mu}$ from Eq. (60)

$$\widehat{\mathbf{P}} = \begin{bmatrix} \mathbf{P}_{00} & \cdots & \mathbf{P}_{0\mu} & \cdots & \mathbf{P}_{0P} \\ \vdots & \ddots & \vdots & \ddots & \vdots \\ \mathbf{P}_{\alpha 0} & \cdots & \mathbf{P}_{\alpha\mu} & \cdots & \mathbf{P}_{\alpha P} \\ \vdots & \ddots & \vdots & \ddots & \vdots \\ \mathbf{P}_{P0} & \cdots & \mathbf{P}_{P\mu} & \cdots & \mathbf{P}_{PP} \end{bmatrix} = \begin{bmatrix} | & & | & & | \\ \widehat{\mathbf{P}}_0 & \cdots & \widehat{\mathbf{P}}_\mu & \cdots & \widehat{\mathbf{P}}_P \\ | & & | & & | \end{bmatrix} , \tag{63}$$

where the $(\mu+1)$-th column of $\widehat{\mathbf{P}}$ is denoted by $\widehat{\mathbf{P}}_\mu \in \mathbb{R}^{ndof \cdot \bar{P}}$. It can be seen that this matrix contains $\bar{P}$ right-hand sides, which depend on the initial external load. In the case of deterministic external loads, $\mathbf{P}_\gamma = \delta_{\gamma 0} \mathbf{P}_0$ holds. Therefore, the individual bloc matrices in Eq. (63) can be written as

$$\mathbf{P}_{\alpha\mu} = D_{\alpha\mu\gamma} \mathbf{P}_\gamma = D_{\alpha\mu\gamma} \delta_{\gamma 0} \mathbf{P}_0 = \delta_{\alpha\mu} \mathbf{P}_0 \,. \tag{64}$$

Hence, the matrix $\widehat{\mathbf{P}}$ simplifies to

$$\widehat{\mathbf{P}} = \mathrm{diag}(\underbrace{\mathbf{P}_0, \ldots, \mathbf{P}_0}_{\bar{P} \text{ times}}) \,, \tag{65}$$

where all off diagonal vectors are equal to zero.

Using the introduced matrices, the complete linearization in Eq. (57) reads

$$\begin{bmatrix} \mathbf{K}_T & -\widehat{\mathbf{P}} \\ \widehat{\mathbf{f}}_\mathrm{v}^T & \mathbf{0} \end{bmatrix} \begin{bmatrix} \Delta\mathbf{v} \\ \Delta\boldsymbol{\lambda} \end{bmatrix} = - \begin{bmatrix} \mathbf{G}(\mathbf{v}, \boldsymbol{\lambda}) \\ \mathbf{f}(\mathbf{v}) \end{bmatrix} \tag{66}$$

$$\text{with} \quad \begin{matrix} \mathbf{K}_T \in \mathbb{R}^{(ndof \cdot \bar{P}) \times (ndof \cdot \bar{P})} \,, & \widehat{\mathbf{P}} \in \mathbb{R}^{(ndof \cdot \bar{P}) \times \bar{P}} \\ \widehat{\mathbf{f}}_\mathrm{v}^T \in \mathbb{R}^{\bar{P} \times (ndof \cdot \bar{P})} \,, & \mathbf{0} \in \mathbb{R}^{\bar{P} \times \bar{P}} \end{matrix} \,.$$

Similar to Eq. (52), all $\bar{P}$ PC coefficients of the increment of the load factor are gathered in the vector $\Delta\boldsymbol{\lambda} \in \mathbb{R}^{\bar{P}}$.

The linearization in Eq. (66) leads in general to a non-symmetric matrix. Consequently, a block elimination method is used to solve this system of equations for the increments $\Delta\mathbf{v}$ and $\Delta\boldsymbol{\lambda}$. Using the first line in Eq. (66), we obtain

$$\mathbf{K}_T \Delta\mathbf{v} = \widehat{\mathbf{P}} \Delta\boldsymbol{\lambda} - \mathbf{G} \,. \tag{67}$$

Partitioning the right-hand side of Eq. (67) in $\widehat{\mathbf{P}}$ and $\mathbf{G}$ leads to two separate equations

$$\mathbf{K}_T \Delta\mathbf{v}^G = -\mathbf{G} \,, \tag{68}$$

$$\mathbf{K}_T \Delta\widehat{\mathbf{v}}^P = \widehat{\mathbf{P}} \,. \tag{69}$$

The displacement increment $\Delta\mathbf{v}^G$ resulting from the residual $\mathbf{G}$ reads

$$\Delta\mathbf{v}^G = \begin{bmatrix} \Delta\mathbf{v}_0^G \\ \vdots \\ \Delta\mathbf{v}_\alpha^G \\ \vdots \\ \Delta\mathbf{v}_P^G \end{bmatrix} \in \mathbb{R}^{ndof \cdot \bar{P}} \,. \tag{70}$$

At this point, it should be noted again that $\widehat{\mathbf{P}}$ is a matrix with $\bar{P}$ columns, see Eq. (63). This results in the increment $\Delta\widehat{\mathbf{v}}^P$ also being a matrix

$$\Delta\widehat{\mathbf{v}}^P = \begin{bmatrix} \Delta\mathbf{v}_{00}^P & \cdots & \Delta\mathbf{v}_{0\alpha}^P & \cdots & \Delta\mathbf{v}_{0P}^P \\ \vdots & \ddots & \vdots & \ddots & \vdots \\ \Delta\mathbf{v}_{\beta 0}^P & \cdots & \Delta\mathbf{v}_{\beta\alpha}^P & \cdots & \Delta\mathbf{v}_{\beta P}^P \\ \vdots & \ddots & \vdots & \ddots & \vdots \\ \Delta\mathbf{v}_{P0}^P & \cdots & \Delta\mathbf{v}_{P\alpha}^P & \cdots & \Delta\mathbf{v}_{PP}^P \end{bmatrix} \in \mathbb{R}^{(ndof \cdot \bar{P}) \times \bar{P}} \tag{71}$$

$$= \begin{bmatrix} | & & | & & | \\ \Delta\widehat{\mathbf{v}}_0^P & \cdots & \Delta\widehat{\mathbf{v}}_\alpha^P & \cdots & \Delta\widehat{\mathbf{v}}_P^P \\ | & & | & & | \end{bmatrix}, \quad \Delta\widehat{\mathbf{v}}_\alpha^P \in \mathbb{R}^{ndof\cdot\bar{P}} .$$

Here, $\Delta\widehat{\mathbf{v}}_\alpha^P$ denotes the $(\alpha+1)$-th column of the matrix $\Delta\widehat{\mathbf{v}}^P$. Equation (69) can also be formulated in terms of the individual right-hand sides

$$\mathbf{K}_T \Delta\widehat{\mathbf{v}}_\alpha^P = \widehat{\mathbf{P}}_\alpha , \quad \forall\alpha \in \{0, \dots, P\} . \tag{72}$$

Taking into account Eqs. (67), (68) and (69), the complete displacement increment is calculated with

$$\Delta\mathbf{v} = \Delta\widehat{\mathbf{v}}^P \Delta\boldsymbol{\lambda} + \Delta\mathbf{v}^G . \tag{73}$$

Considering the second line in Eq. (66), we get

$$\widehat{\mathbf{f}}_{\mathrm{v}}^T \Delta\mathbf{v} + \mathbf{0} = -\mathbf{f}(\mathbf{v}) . \tag{74}$$

Due to the linear constraint, $\mathbf{f}(\mathbf{v}) = \mathbf{0}$ holds. By substituting the expression for $\Delta\mathbf{v}$ in Eq. (73) into Eq. (74), one obtains

$$\widehat{\mathbf{f}}_{\mathrm{v}}^T \left(\Delta\widehat{\mathbf{v}}^P \Delta\boldsymbol{\lambda} + \Delta\mathbf{v}^G \right) = \widehat{\mathbf{f}}_{\mathrm{v}}^T \Delta\widehat{\mathbf{v}}^P \Delta\boldsymbol{\lambda} + \widehat{\mathbf{f}}_{\mathrm{v}}^T \Delta\mathbf{v}^G = \mathbf{0} . \tag{75}$$

At this point, it is reasonable to define the following quantities

$$\Delta\widehat{\mathbf{v}}^{P,\mathrm{c}} := \widehat{\mathbf{f}}_{\mathrm{v}}^T \Delta\widehat{\mathbf{v}}^P \quad \text{and} \quad \Delta\mathbf{v}^{G,\mathrm{c}} := \widehat{\mathbf{f}}_{\mathrm{v}}^T \Delta\mathbf{v}^G . \tag{76}$$

As shown in Eq. (59), the matrix $\widehat{\mathbf{f}}_{\mathrm{v}}^T$ only consists of zeros and ones. Therefore, the matrix $\Delta\widehat{\mathbf{v}}^{P,\mathrm{c}}$ and vector $\Delta\mathbf{v}^{G,\mathrm{c}}$ defined in Eq. (76), are written as

$$\Delta\widehat{\mathbf{v}}^{P,\mathrm{c}} = \begin{bmatrix} \Delta v_{00}^{P,\mathrm{c}} & \cdots & \Delta v_{0\alpha}^{P,\mathrm{c}} & \cdots & \Delta v_{0P}^{P,\mathrm{c}} \\ \vdots & \ddots & \vdots & \ddots & \vdots \\ \Delta v_{\beta 0}^{P,\mathrm{c}} & \cdots & \Delta v_{\beta\alpha}^{P,\mathrm{c}} & \cdots & \Delta v_{\beta P}^{P,\mathrm{c}} \\ \vdots & \ddots & \vdots & \ddots & \vdots \\ \Delta v_{P0}^{P,\mathrm{c}} & \cdots & \Delta v_{P\alpha}^{P,\mathrm{c}} & \cdots & \Delta v_{PP}^{P,\mathrm{c}} \end{bmatrix} \in \mathbb{R}^{\bar{P}\times\bar{P}} \tag{77}$$

and

$$\Delta\mathbf{v}^{G,\mathrm{c}} = \left[\Delta v_0^{G,\mathrm{c}}, \dots, \Delta v_\beta^{G,\mathrm{c}}, \dots, \Delta v_P^{G,\mathrm{c}} \right]^T \in \mathbb{R}^{\bar{P}} . \tag{78}$$

Here, the superscript $(\bullet)^{\mathrm{c}}$ indicates the association with the prescribed displacement quantity v^{c}. Taking into account Eq. (76), Eq. (75) is rewritten as

$$\Delta\widehat{\mathbf{v}}^{P,\mathrm{c}} \Delta\boldsymbol{\lambda} + \Delta\mathbf{v}^{G,\mathrm{c}} = \mathbf{0} . \tag{79}$$

Finally, the increment of the load factor $\Delta\boldsymbol{\lambda}$ is obtained from

$$\Delta\boldsymbol{\lambda} = -(\Delta\widehat{\mathbf{v}}^{P,\mathrm{c}})^{-1} \Delta\mathbf{v}^{G,\mathrm{c}} . \tag{80}$$

Algorithm 3 shows a schematic flowchart of the generalized displacement control used in a finite element program.

Algorithm 3 Generalized displacement control

```
λ_0^(1) = 0, v_0^(1) = 0, v̄^c                                   ▷ Initialization
for n = 1, ..., N do                                            ▷ Load loop
  i = 0
  while ||G|| > TOL do                                          ▷ NEWTON loop
    for e = 1, ..., numel do                                    ▷ Element loop
      g^e and k_T^e                                             ▷ Element residual and tangent
      K_T ← K_T + ⋃_e k_T^e,  G ← G + ⋃_e g^e                   ▷ Assembly
    end for
    if i = 0 then
      K_T Δv̂_i^P = P̂
      Δλ_i^(n) = (Δv̂_i^{P,c})^{-1} Δv̄^c                         ▷ Increment load factor
      Δv_i^(n) = Δv̂_i^P Δλ_i^(n)                                ▷ Displacement increment
    else
      K_T Δv̂_i^P = P̂,  K_T Δv_i^G = −G
      Δλ_i^(n) = −(Δv̂_i^{P,c})^{-1} Δv_i^{G,c}                  ▷ Increment load factor
      Δv_i^(n) = Δv̂_i^P Δλ_i^(n) + Δv_i^G                       ▷ Displacement increment
    end if
    v_{i+1}^(n) = v_i^(n) + Δv_i^(n)                            ▷ Update displacements
    λ_{i+1}^(n) = λ_i^(n) + Δλ_i^(n)                            ▷ Update load factor
    i ← i + 1
  end while
  v_i^(n+1) = v_i^(n),  λ_i^(n+1) = λ_i^(n)
end for
```

Illustrative example

As an illustrative example of the proposed generalized displacement control, the kinked beam under a stochastic dead load shown in Fig. 5 is considered. The beam has a rectangular cross-section and the shear correction factor is $\kappa = 5/6$.

The Young's modulus is modeled as normal distributed random variable

$$E(\omega) \sim \mathcal{N}(1000, 100)\ \mathrm{kN/cm^2} . \tag{81}$$

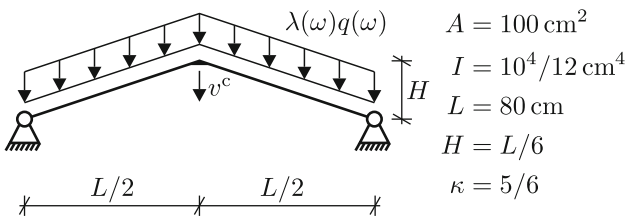

Fig. 5 Kinked beam under dead load: system and geometry

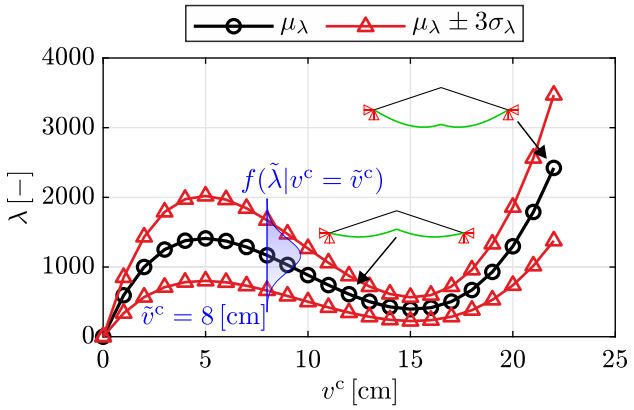

Fig. 6 Stochastic load factor λ versus the deterministic displacement v^c and a qualitative PDF of the load factor $\tilde{\lambda}$ at the load level $\tilde{v}^c = 8\,\text{cm}$

Similar to the previous illustrative examples, the shear modulus is modeled as $G(\omega) = E(\omega)/2$. Furthermore, the uncertain dead load $q(\omega)$ is quantified by a normal distribution

$$q(\omega) \sim \mathcal{N}(0.015,\ 0.0015)\,\text{kN/cm}\ . \tag{82}$$

The spatial and stochastic discretization are equivalent to the principle example in Sect. 4.2. Similarly to the previous example, the displacement v^c is increased with an increment of $\Delta v^c = 1\,\text{cm}$. Here, 22 load steps are used. It should be noted again, that the controlled displacement v^c is deterministic.

Due to the stochastic modeling of the material properties and the dead load, the load factor is a stochastic quantity. Figure 6 shows the mean value μ_λ of the stochastic load factor versus the prescribed displacement v^c.

To illustrate the variation of the random load factor λ, the mean value μ_λ plus minus three times the standard deviation σ_λ is shown. For a given value of the prescribed displacement $\tilde{v}^c = 8\,\text{cm}$, the corresponding stochastic load factor is $\tilde{\lambda}$. In addition, a qualitative PDF $f(\tilde{\lambda}|v^c = \tilde{v}^c)$ of the load factor at the displacement state $\tilde{v}^c = 8\,\text{cm}$ is depicted in Fig. 6.

5.2 Consistency of the generalized displacement control

When no uncertainty is considered in the structural analysis, the relationships shown in Sect. 5 can be simplified. When all parameters are deterministic, the submatrices $\mathbf{K}_{T\alpha\beta}$ in Eq. (34) and the subvectors $\mathbf{P}_{\alpha\mu}$ in Eq. (63) reduce to

$$\mathbf{K}_{T\alpha\beta} = \delta_{\alpha\beta}\mathbf{K}_{T00}\ , \quad \mathbf{P}_{\alpha\mu} = \delta_{\alpha\mu}\mathbf{P}_0\ . \tag{83}$$

This leads to the fact, that the global stiffness matrix $\mathbf{K}_T$ and the matrix $\widehat{\mathbf{P}}$ have a block diagonal form

$$\mathbf{K}_T = \text{diag}(\underbrace{\mathbf{K}_{T00}, \ldots, \mathbf{K}_{T00}}_{\bar{P}\ \text{times}})\ , \quad \widehat{\mathbf{P}} = \text{diag}(\underbrace{\mathbf{P}_0, \ldots, \mathbf{P}_0}_{\bar{P}\ \text{times}})\ . \tag{84}$$

The global residual vector $\mathbf{G}$ in Eq. (68) is nonzero only for the first PC coefficient.

$$\mathbf{G} = \left[\mathbf{G}_0^T, \ldots, \mathbf{0}, \ldots, \mathbf{0}\right]^T\ . \tag{85}$$

Taking into account Eq. (84), it follows from Eq. (69) that the matrix $\Delta\widehat{\mathbf{v}}^P$ also has a block diagonal form

$$\Delta\widehat{\mathbf{v}}^P = \text{diag}(\underbrace{\Delta\mathbf{v}_{00}^P, \ldots, \Delta\mathbf{v}_{00}^P}_{\bar{P}\ \text{times}})\ . \tag{86}$$

Considering Eqs. (84) and (85), the displacement increment in Eq. (68) simplifies to

$$\Delta\mathbf{v}^G = \left[(\Delta\mathbf{v}_0^G)^T, \ldots, \mathbf{0}, \ldots, \mathbf{0}\right]^T\ . \tag{87}$$

The previous simplifications apply analogously to the two quantities defined in Eq. (76)

$$\Delta\widehat{\mathbf{v}}^{P,c} = \begin{bmatrix} \Delta v_{00}^{P,c} & \ldots & \mathbf{0} \\ \vdots & \ddots & \vdots \\ \mathbf{0} & \ldots & \Delta v_{00}^{P,c} \end{bmatrix}\ , \quad \Delta\mathbf{v}^{G,c} = \begin{bmatrix} \Delta v_0^{G,c} \\ \vdots \\ \mathbf{0} \end{bmatrix}\ . \tag{88}$$

It follows from Eq. (80), that only the first PC coefficient of the increment $\Delta\boldsymbol{\lambda}$ is non-zero. This leads to the fact, that the increment and finally the load factor $\boldsymbol{\lambda}$ itself is a deterministic quantity. Thus, the proposed generalized displacement control corresponds to the procedure described in [25], independent of the chosen polynomial degree of the PC expansion.

5.3 Concluding remarks

The generalized displacement control, offers some advantages compared to the solution algorithms described in Sects. 4.1 and 4.2.

- Using the generalized displacement control, structures can be investigated under various loading conditions. Examples of these are single and line loads, surface tractions, and body forces.

- The degree of freedom to be controlled during the solution algorithm can be selected independently of the external load.
- The proposed solution algorithm allows stochastic external loads to be taken into account.
- The prescribed displacement quantity can be changed within the solution algorithm.

In addition to the advantages mentioned, the proposed algorithm also has a limitation.

- Within the calculation, the prescribed displacement quantity typically increases. Therefore, a snap-back behavior, which sometimes occurs in stability problems, cannot be treated.

6 Implementation of the SSFEM into a general finite element analysis program

This section provides insights into the implementation of the SSFEM within a finite element program. A general purpose FE program such as FEAP [22] can be used to implement the described solution algorithms in Sects. 4 and 5.

First of all, we present the overall structure of such a program, which provides the basis for the implementation. Subsequently, the vectors and matrices required for the implementation of stochastic FE formulations are described, as outlined in Sect. 3. For the sake of completeness, Appendix C provides a comprehensive element routine for a two-dimensional stochastic geometrically nonlinear solid element.

6.1 General purpose FE program for SSFEM calculations

The flowchart of a general purpose FE program is shown in Fig. 7. All blue boxes in Fig. 7 represent additional tasks within the overall structure that are essential for the SSFEM calculation. The illustration clearly shows that most of the overall structure remains unchanged despite the incorporation of the SSFEM. Furthermore, the red boxes highlight the principal modifications required for the generalized displacement control described in Sect. 5.

At the beginning, all random input parameters of the vector $\mathbf{X}(\omega) \in \mathbb{R}^M$ in Eq. (2) with the corresponding joint PDF $f_{\mathbf{X}}(\mathbf{x})$ in Eq. (3) have to be defined. Furthermore, the user has to choose a maximum polynomial degree $p \in \mathbb{N}$ as well as a q-norm $q \in (0, 1]$ for the underlying M-dimensional PC expansion. For a more detailed description of the q-norm and its effect on the size of the polynomial basis, the reader is referred to, e.g., [5]. Based on the defined random input variables, all components of the multiplication tensor $D_{\alpha\beta\gamma}$

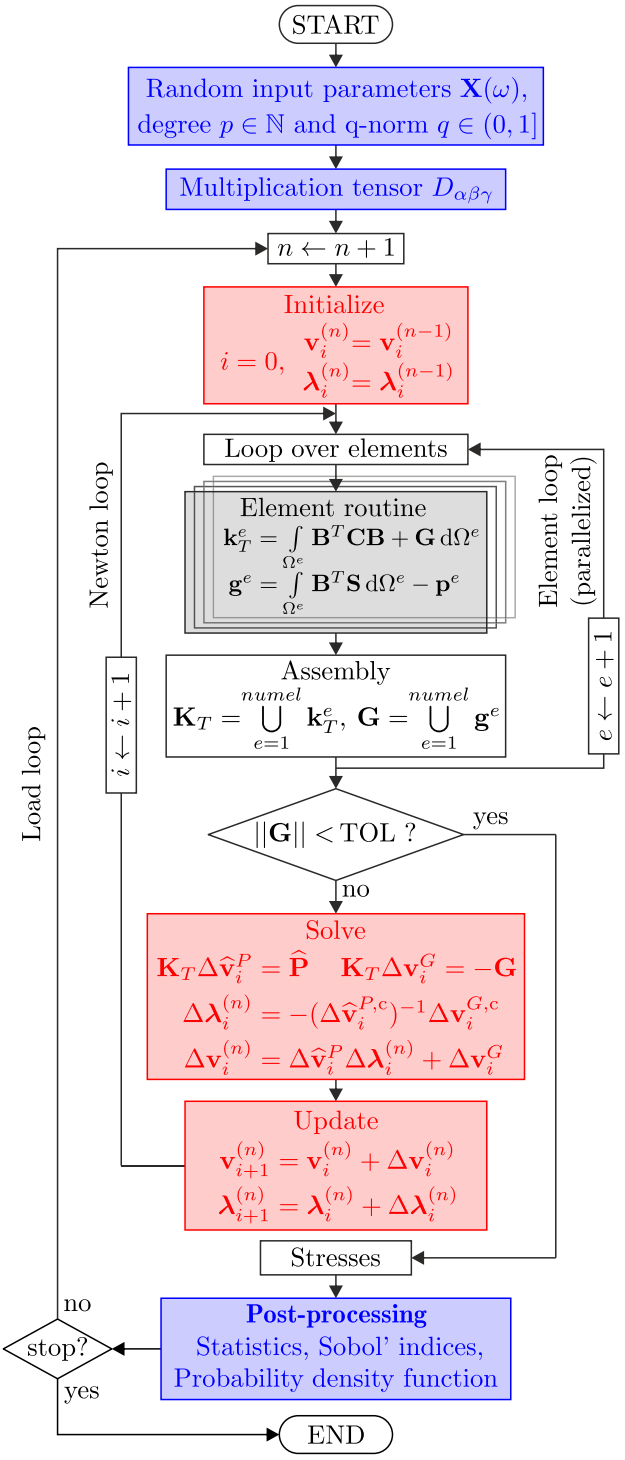

Fig. 7 Flowchart of a modified incremental-iterative finite element program for SSFEM calculations

are calculated. This step is only necessary once, since the tensor $D_{\alpha\beta\gamma}$ does not change during the entire computation.

Depending on the solution algorithm at hand, the external load or a prescribed displacement is incrementally increased within the load loop. Figure 7 illustrates the proposed

generalized displacement control described in Sect. 5, and therefore a user-defined displacement quantity is controlled.

For the Newton iteration within each load step, the current global residual $\mathbf{G}$, the external load $\widehat{\mathbf{P}}$, and the tangent stiffness matrix $\mathbf{K}_T$ are required to calculate the actual displacement increment $\Delta \mathbf{v}_i^{(n)}$ and the increment of the load factor $\Delta \boldsymbol{\lambda}_i^{(n)}$, see Eqs. (73) and (80). Within the element loop, the individual element arrays $\mathbf{g}^e$ and $\mathbf{k}_T^e$ are computed for each element $e = 1, \ldots, numel$. A detailed description of an element routine is provided in Appendix C. This process can be performed in parallel, as shown in Figure 7. The assembling of all element-related arrays finally leads to the global residual vector $\mathbf{G}$ and the global stiffness matrix $\mathbf{K}_T$, as described in Sect. 3. Once the next equilibrium point has been reached, additional quantities of interest such as stresses can be calculated in addition to the displacements.

As part of an SSFEM calculation, an additional step is carried out to post-process the results, see the blue box at the bottom in Fig. 7. This includes the computation of stochastic moments, Sobol' indices, and the probability density function (PDF) of a defined quantity of interest. For a detailed discussion of this post-processing step, see [20, 21].

6.2 Definition of arrays at the element level

Within the overall computation, the residual $\mathbf{g}^e$ and the corresponding tangent stiffness matrix $\mathbf{k}_T^e$ are calculated for each element $e = 1, \ldots, numel$. This section provides a detailed description and definition of these element-related arrays.

The stochastic displacement field is discretized with

$$\mathbf{u} = \sum_{\alpha} \sum_{I} \Psi_\alpha N_I \mathbf{v}_{I\alpha} \,, \quad \alpha = 0, \ldots, P \,, \quad I = 1, \ldots, nel \,, \tag{89}$$

where $\mathbf{v}_{I\alpha} \in \mathbb{R}^{ndf}$ is the α-th PC coefficient of the nodal displacements of node I. Here, ndf denotes the deterministic number of degrees of freedom of a single nodal point. All PC coefficients of the displacement quantities associated with a single node I are arranged in the vector

$$\mathbf{v}_I = \left[\mathbf{v}_{I0}^T, \ldots, \mathbf{v}_{I\alpha}^T, \ldots, \mathbf{v}_{IP}^T\right]^T \in \mathbb{R}^{ndf \cdot \bar{P}} \,. \tag{90}$$

Combining the displacement arrays $\mathbf{v}_I$ for all nel nodes of one element e yields the element displacement vector

$$\mathbf{v}^e = \left[\mathbf{v}_1, \ldots, \mathbf{v}_I^T, \ldots, \mathbf{v}_{nel}^T\right]^T \in \mathbb{R}^{nst \cdot \bar{P}} \,, \tag{91}$$

where $nst = nel \cdot ndf$.

The nodal part $\mathbf{g}_I$ of the residual vector and the residual $\mathbf{g}^e$ at the element level are defined in the same manner

$$\begin{aligned} \mathbf{g}_I &= \left[\mathbf{g}_{I0}^T, \ldots, \mathbf{g}_{I\alpha}^T, \ldots, \mathbf{g}_{IP}^T\right]^T \in \mathbb{R}^{ndf \cdot \bar{P}} \,, \\ \mathbf{g}^e &= \left[\mathbf{g}_1, \ldots, \mathbf{g}_I, \ldots, \mathbf{g}_{nel}\right]^T \in \mathbb{R}^{nst \cdot \bar{P}} \,. \end{aligned} \tag{92}$$

Furthermore, the element tangent stiffness matrix $\mathbf{k}_T^e$ is written as

$$\mathbf{k}_T^e = \begin{bmatrix} \mathbf{k}_{T11} & \cdots & \mathbf{k}_{T1nel} \\ \vdots & \mathbf{k}_{TIK} & \vdots \\ \mathbf{k}_{Tnel1} & \cdots & \mathbf{k}_{Tnelnel} \end{bmatrix} \in \mathbb{R}^{(nst \cdot \bar{P}) \times (nst \cdot \bar{P})}, \tag{93}$$

where each nodal part $\mathbf{k}_{TIK}$ is defined as

$$\mathbf{k}_{TIK} = \begin{bmatrix} \mathbf{k}_{TIK00} & \cdots & \mathbf{k}_{TIK0P} \\ \vdots & \mathbf{k}_{TIK\alpha\beta} & \vdots \\ \mathbf{k}_{TIKP0} & \cdots & \mathbf{k}_{TIKPP} \end{bmatrix} \in \mathbb{R}^{(ndf \cdot \bar{P}) \times (ndf \cdot \bar{P})}. \tag{94}$$

Due to the symmetry properties of the multiplication tensor $D_{\alpha\beta\gamma}$, the symmetry of $\mathbf{k}_{TIK}$ and consequently that of $\mathbf{k}_T^e$ is retained.

The element-related vectors and matrices introduced in this section form the basis for implementing spectral stochastic FE formulations of various structural elements. To provide further insight into the implementation, an element routine for a two-dimensional solid element is presented in Appendix C.

7 Numerical examples

7.1 Layered cylindrical shell

First, we investigate a layered cylindrical shell, depicted in Fig. 8, which is as a typical numerical example in geometrically nonlinear shell analysis, see e.g. [9]. The structure is clamped at $x_2 = L$ and free at $x_2 = 0$. Due to the symmetry of both, the entire system and the external load, only one quarter of the shell is considered.

Therefore, symmetry boundary conditions are imposed at $x_1 = 0$ and $x_3 = 0$. The layer sequence of the shell is $[0°/90°/0°]$, with each layer having a thickness of $h/3$, where h is the total thickness of the shell. Here, $0°$ refers to the circumferential, and $90°$ to the longitudinal direction of the cylindrical shell.

For the probabilistic calculation, we consider uncertainties in the line load $q_0(x_2, \omega)$ and in the material properties. The external load acting on the symmetrized system is modeled as a one-dimensional spatially correlated Gaussian random field

$$q_0(x_2, \omega) \sim \mathcal{N}(1, 0.1)\,\text{N/mm}\,. \tag{95}$$

Furthermore, we choose the squared exponential correlation function

$$\rho(\boldsymbol{x}_i, \boldsymbol{x}_k) = \exp\left(-\frac{d^2(\boldsymbol{x}_i, \boldsymbol{x}_k)}{\ell_c}\right) \tag{96}$$

with a correlation length of $\ell_c = 200$ mm. Here, $d(\boldsymbol{x}_i, \boldsymbol{x}_k) = \|\boldsymbol{x}_i - \boldsymbol{x}_k\|_2$ denotes the euclidean distance between the two spatial points $\boldsymbol{x}_i$ and $\boldsymbol{x}_k$. To discretize the random field, we use the Karhunen–Loève expansion (KLE), see e.g. [19].

In order to reduce the number of terms in the KLE, a value of $Q = 0.99$ is chosen for the quality measure, see Appendix A. With this choice, only $K = 4$ of the total $N = 21$ random variables remain to describe the spatially correlated field, where $N = 21$ corresponds to the number of nodal points on the loaded edge. These four random variables are $\theta_1, \ldots, \theta_4$, which all follow a standard normal distribution. The representation of the discretized random field using the PCE is provided in Appendix A. Figure 9 depicts five random realizations of the spatially varying line load $q_0(x_2, \omega)$.

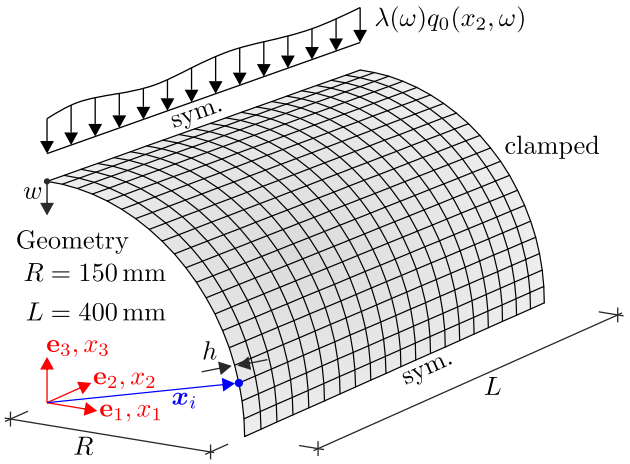

Fig. 8 Layered cylindrical shell: system, geometry, boundary conditions and external load

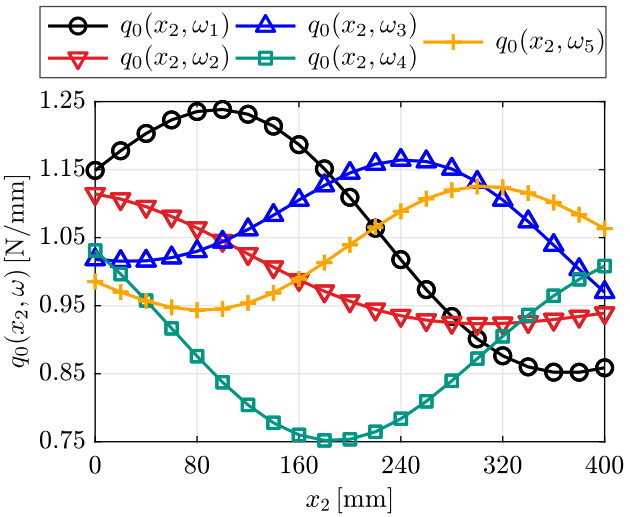

Fig. 9 Five random realizations of the stochastic line load $q_0(x_2, \omega)$

In addition to the random line load $q_0(x_2, \omega)$,we model the Young's moduli $E_1(\omega)$ and $E_2(\omega)$ as two independent normal distributed random variables with the properties

$$\begin{aligned} E_1 &\sim \mathcal{N}(125000, 12500)\,\text{N/mm}^2\,, \\ E_2 &\sim \mathcal{N}(7400, 740)\,\text{N/mm}^2\,. \end{aligned} \tag{97}$$

Finally, all $M = 6$ random variables are summarized in the input vector

$$\begin{aligned} \mathbf{X}(\omega) &= [X_1,\ X_2,\ X_3,\ X_4,\ X_5,\ X_6]^T \\ &= [\theta_1,\ \theta_2,\ \theta_3,\ \theta_4,\ E_1,\ E_2]^T \in \mathbb{R}^6\,. \end{aligned} \tag{98}$$

For the remaining material parameters we choose the following deterministic values according to [9]

$$G_{12} = 4800\,\text{N/mm}^2\,,\quad G_{23} = 2700\,\text{N/mm}^2\,,\quad \nu_{12} = 0.34\,. \tag{99}$$

For the numerical simulation, the structure is discretized with 20×20 quadrilateral shell elements. The corresponding stochastic shell formulation is similar to that proposed in [13]. The discretization of the structure, shown in Fig. 8, results in 2020 degrees of freedom in the deterministic case, considering the boundary conditions presented. The choice of the polynomial degree p and the q-norm q directly influences the number of the resulting degrees of freedom as shown in Table 1.

In the simulation the displacement quantity w at $(0, 0, R)$, see Fig. 8, is increased in steps of $\Delta w = 1$ mm from 0 to 15 mm. Within the solution algorithm, the $\bar{P}$ PC coefficients $\lambda_\alpha, \alpha \in \{0, \ldots, P\}$ of the load factor associated with the stochastic line load $q_0(x_2, \omega)$ are calculated.

At this point it should be noted, that due to the stochastic external load, the matrix $\widehat{\mathbf{P}}$ in Eq. (63) does not exhibit a block-diagonal structure. As shown in Fig. 10, it is obvious that the load factor λ increases monotonically with increasing values of the displacement w. For this reason, it is also possible to trace the equilibrium path of the structure using the load control described in Sect. 4.1. However, this solution algorithm will not be examined further in this numerical example.

7.1.1 Results of the SSFEM

In order to obtain converged results with the Monte Carlo simulation, a total of $N = 5 \times 10^5$ samples are used. The sub-

Table 1 Settings for SSFEM computation, notation, number of basis polynomials $\tilde{P}$ and degrees of freedom $ndof \cdot \tilde{P}$

Settings	Notation	$\tilde{P}$	$ndof \cdot \tilde{P}$
$p = 1/q = 1$	sfem p1q1	7	14140
$p = 2/q = 1$	sfem p2q1	28	56560
$p = 3/q = 1$	sfem p3q1	84	169680
$p = 4/q = 0.8$	sfem p4q0.8	90	181800

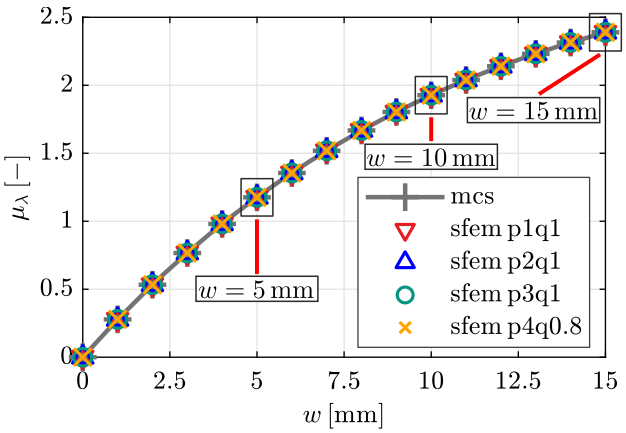

Fig. 10 Mean value μ_λ of the load factor λ for different combinations of the polynomial degree p and the q-norm q

sequent figures illustrate the first three stochastic moments of the random load factor λ versus the deterministic controlled displacement w.

As shown in Fig. 10, all SSFEM configurations given in Table 1 show excellent agreement for the mean value μ_λ of the load factor λ with the results obtained from the MCS. Furthermore, it can be observed that the shell structure softens with increasing external load.

For the standard deviation σ_λ, depicted in Fig. 11, the SSFEM shows a similar approximation behavior. Moreover, the mean value μ_λ in Fig. 10 and the standard deviation σ_λ in Fig. 11 exhibit a qualitatively similar trend.

In order to assess the relative variability of the load factor λ, the coefficient of variation $v_\lambda = \sigma_\lambda / \mu_\lambda$ is shown in Fig. 12. Here, the minor deviation of the SSFEM configuration sfem p1q1 can be clearly seen. The increasing value of v_λ results from the fact that the structure becomes softer as the load increases.

It is obvious from Fig. 13 that a linear chaos expansion, i.e., the configuration sfem p1q1, is not able to capture the skewness δ_λ of the load factor λ. With increasing polynomial degree, the results of the SSFEM converge towards the reference solution obtained with the MCS. Figure 13 also illustrates that the skewness of the load factor λ varies only slightly during the calculation.

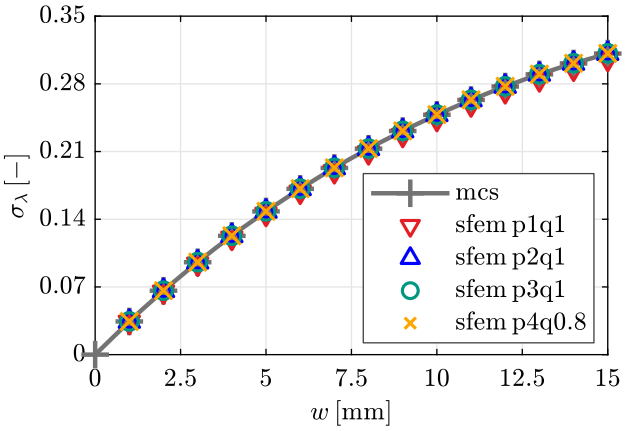

Fig. 11 Standard deviation σ_λ of the load factor λ for different combinations of the polynomial degree p and the q-norm q

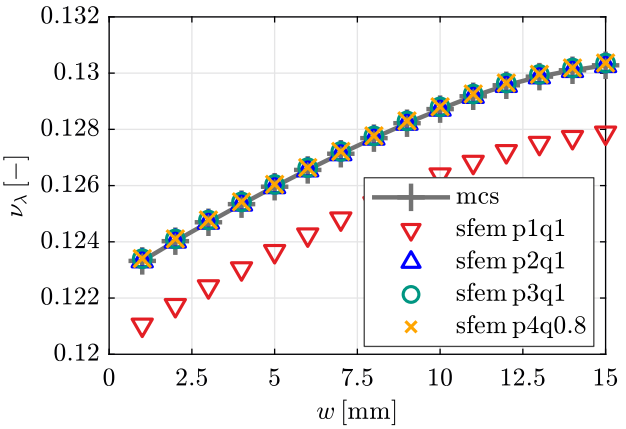

Fig. 12 Coefficient of variation v_λ of the load factor λ for different combinations of the polynomial degree p and the q-norm q

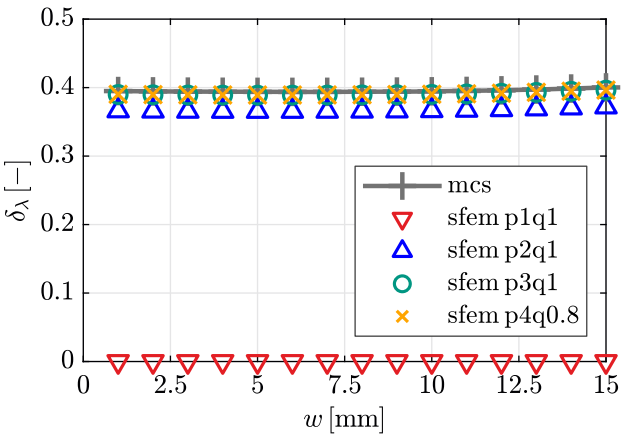

Fig. 13 Skewness δ_λ of the load factor λ for different combinations of the polynomial degree p and the q-norm q

Appendix D contains further investigations of the stochastic load factor λ at the displacement level $w = 15$ mm. In addition to the convergence behavior of the MCS with respect

Table 2 Convergence behavior for the displacement step $w = 14\,\text{mm} \rightarrow 15\,\text{mm}$

No. of iter	sfem p2q1	sfem p3q1	sfem p4q0.8
1	8.818E+01	8.818E+01	8.818E+01
2	3.277E+02	3.278E+02	3.278E+02
3	1.276E−01	1.284E−01	1.284E−01
4	1.677E−03	2.094E−03	2.129E−03
5	3.469E−08	3.264E−08	3.843E−08

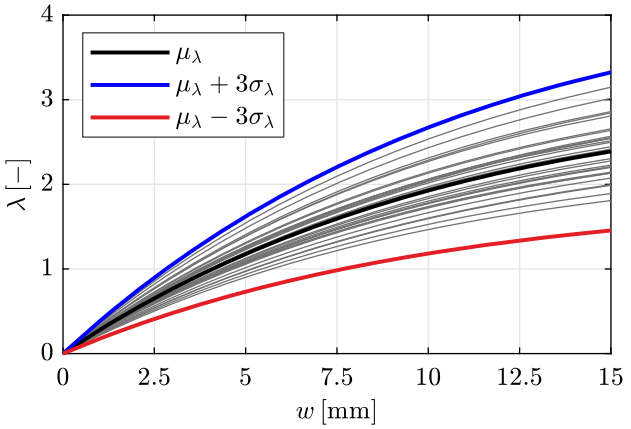

Fig. 14 Mean value μ_λ plus minus three times the standard deviation σ_λ as well as random realizations of the load–displacement curves

to the number of samples, the approximation quality of the SSFEM is also investigated.

For the final displacement step $w = 14\,\text{mm} \rightarrow 15\,\text{mm}$, the convergence behavior is examined in more detail. Table 2 shows the norm of the global residual vector $\mathbf{G}$ for three different configurations of the SSFEM. Within the Newton iteration, a quadratic convergence behavior is observed, which is due to the consistent linearization of all governing equations. Similar results apply to the configuration sfem p1q1, which is not shown here.

To illustrate the variation of the stochastic load factor, the mean value μ_λ plus minus three times the standard deviation σ_λ is depicted in Fig. 14. Additionally, multiple random load–displacement curves are shown. This figure clearly demonstrates the impact of the stochastic modeling of the line load $q_0(x_2, \omega)$ as well as the Young's moduli $E_1(\omega)$ and $E_2(\omega)$ on the response of the shell structure.

7.1.2 Sensitivity analysis

In the following, the influence of the $M = 6$ input variables on the variability of the stochastic load factor λ is investigated. To this end, the total PCE-based Sobol' indices are considered at the three displacement levels $w = 5\,\text{mm}$, $w = 10\,\text{mm}$, and $w = 15\,\text{mm}$, as indicated in Fig. 10. The total

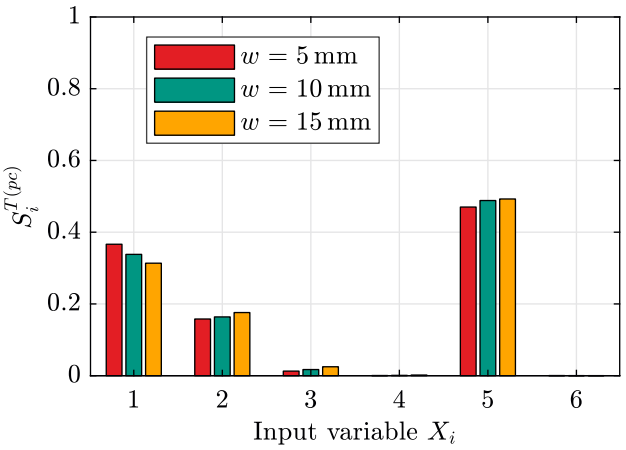

Fig. 15 Total PCE-based Sobol' indices $S_i^{T(pc)}$ for the three displacement levels $w = 5\,\text{mm}$, $w = 10\,\text{mm}$ and $w = 15\,\text{mm}$

PCE-based Sobol' indices shown in Fig. 15 are determined based on the configuration sfem p4q0.8.

It can be seen that the sensitivity index of each variable shows only slight variations across all three displacement levels. In contrast to this, significant differences are noticeable in the total PCE-based Sobol' indices $S_i^{T(pc)}, i = 1, \ldots, 6$ among the different input variables. The decreasing influence of the first four input variables $X_i, i = 1, \ldots, 4$ results from the decreasing magnitude of the eigenvalues $\lambda_i, i = 1, \ldots, 4$ in the KLE, see Appendix A.

Furthermore, it becomes evident that the input variable $X_5 = E_1$ has a significantly greater influence than the variable $X_6 = E_2$. The minor influence arises from the layer sequence $[0°/90°/0°]$ and the structural behavior of the shell. The primary load-bearing direction corresponds to the circumferential one, where the two outer layers with a fiber angle of 0° significantly affect the stiffness of the structure with the Young's modulus E_1.

7.1.3 Probability density function

Finally, we examine the probability density function (PDF) $f_\lambda(\lambda | w = 15\,\text{mm})$ of the load factor λ at the displacement state $w = 15\,\text{mm}$ in more detail. To estimate the PDF from a set of random samples, we use the MATLAB function *ksdensity*. A set of $N = 5 \times 10^5$ realizations of the random vector $\mathbf{X}(\omega)$ in Eq. (98) is used to perform an MCS with both the full FE model and the surrogate model provided by the SSFEM calculation. The reference solution obtained using the FE model is denoted by mcs + fem.

The results of the estimated probability density function are depicted in Fig. 16.

The results of the SSFEM shown in Fig. 16 (top) clearly demonstrate that a linear polynomial basis, i.e., the configuration sfem p1q1, is insufficient to accurately represent the

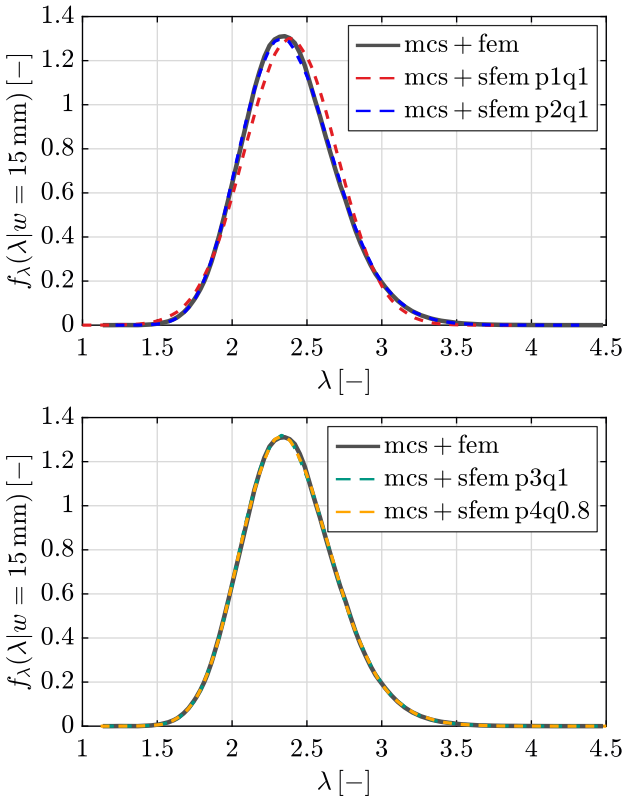

Fig. 16 Probability density function (PDF) $f_\lambda(\lambda|w = 15\,\text{mm})$ of the load factor λ at the displacement level $w = 15\,\text{mm}$

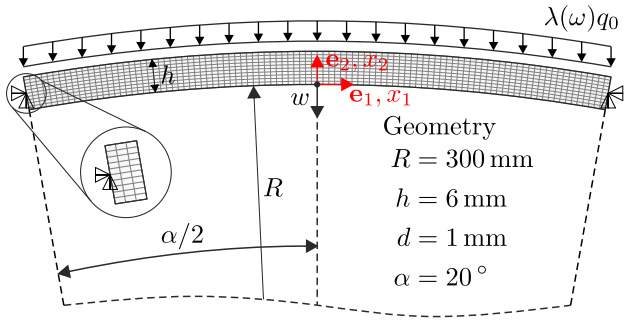

Fig. 17 Arch beam: system, geometry, boundary conditions and external load

distribution of the load factor λ. As becomes clear from Fig. 16 (bottom), increasing the polynomial basis leads to a very accurate approximation of the estimated probability density function.

7.2 Arch beam

Another example for the application of the generalized displacement control, described in Sect. 5, is an arch beam under a constant edge load q_0 as shown in Fig. 17. The arch is simply supported at the left and right ends.

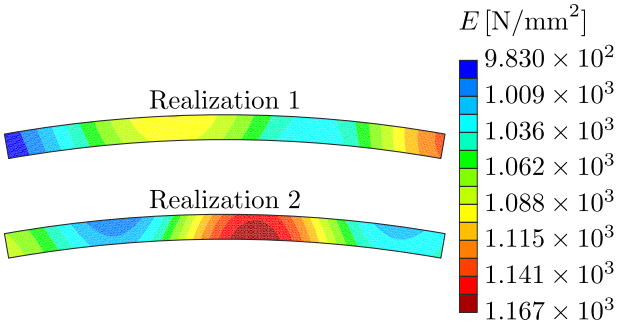

Fig. 18 Two random realizations of the Young's modulus distribution

For the numerical simulation, the structure is discretized using 10 and 100 quadrilateral elements in the radial and circumferential direction, respectively. The mixed-hybrid element formulation used in this example is based on a two-field variational principle originally proposed by [15]. To enable its application in the SSFEM, the deterministic element formulation has been appropriately extended to the stochastic setting.

A plane stress condition is assumed. Furthermore, the material is isotropic and linear elastic. The Young's modulus of the structure is modeled as a spatially correlated Gaussian random field with the properties

$$E(\boldsymbol{x}, \omega) \sim \mathcal{N}(1000, 100)\,\text{N/mm}^2\,. \tag{100}$$

The Poisson's ratio of the material is $\nu = 0.25$. For the random field a squared exponential correlation function

$$\rho(\boldsymbol{x}_i, \boldsymbol{x}_k) = \exp\left(-\frac{d^2(\boldsymbol{x}_i, \boldsymbol{x}_k)}{\ell_c}\right) \tag{101}$$

is used, similar to the example in Sect. 7.1. The correlation length is set to $\ell_c = 30\,\text{mm}$. The Karhunen-Loève expansion is used to discretize the spatially correlated random field, see e.g. [19]. In order to reduce the number of terms in the KLE, a value of $Q = 0.99$ is chosen for the quality measure. Therefore, only $K = 7$ random variables are necessary to describe the random field. Figure 18 depicts two random realizations of the Young's modulus distribution.

The random input vector $\mathbf{X}(\omega) = [\theta_1, \ldots, \theta_7]^T$ summarizes all stochastic input parameters. Each variable $\theta_i, i = 1, \ldots, 7$ is a standard normal distribution. Therefore, Hermite polynomials are used to approximate the stochastic dimension.

Four different combinations of the polynomial degree p and the q-norm q are used for the computation with the SSFEM. Table 3 shows the configurations of the SSFEM and the resulting number of degrees of freedom.

Figure 19 illustrates that the structure undergoes snap-through behavior. Therefore, the generalized displacement

Table 3 Settings for SSFEM computation, notation, number of basis polynomials $\bar{P}$ and degrees of freedom $ndof \cdot \bar{P}$

Settings	Notation	$\bar{P}$	$ndof \cdot \bar{P}$
$p = 1/q = 1$	sfem p1q1	8	17744
$p = 2/q = 1$	sfem p2q1	36	79848
$p = 3/q = 1$	sfem p3q1	120	266160
$p = 4/q = 0.7$	sfem p4q0.7	92	204056

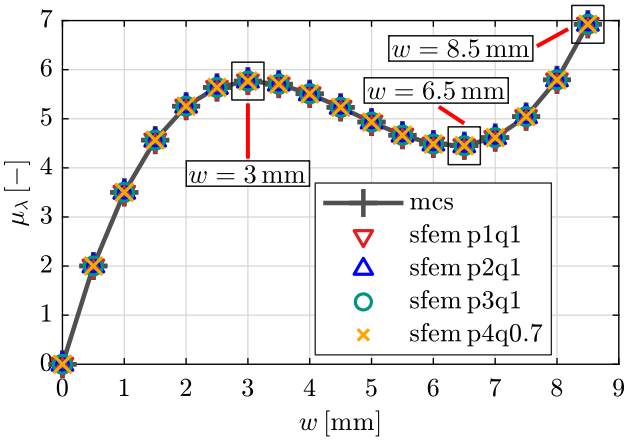

Fig. 19 Mean value μ_λ of the load factor λ for different combinations of the polynomial degree p and the q-norm q

control, described in Sect. 5, is used to trace the nonlinear equilibrium path. The center displacement w, depicted in Fig. 17, is increased in steps of $\Delta w = 0.5$ mm from 0 to 8.5 mm. Within the solution algorithm, the PC coefficients $\lambda_\alpha, \alpha \in \{0, \ldots, P\}$ associated with the deterministic edge load q_0 are calculated.

7.2.1 Results of the SSFEM

First, the results of the different SSFEM configurations in Table 3 are compared with those of a Monte Carlo simulation. In order to get converged results with the MCS, a total of $N = 5 \times 10^5$ samples are used. The following figures depict the first three stochastic moments of the random load factor λ versus the deterministic controlled center displacement w.

It can be seen from Fig. 19, that the mean value μ_λ of the load factor λ is already represented almost exactly by a linear polynomial basis.

In order to illustrate the snap-through of the structure, Fig. 20 depicts the mean value of the deformed structure for the two different displacement states $w = 3$ mm and $w = 6.5$ mm. A similar approximation behavior of the SSFEM is observed for the standard deviation σ_λ of the load factor, see Fig. 21.

Figure 22 clearly shows that the SSFEM is also able to capture the skewness of the stochastic load factor λ. It can be

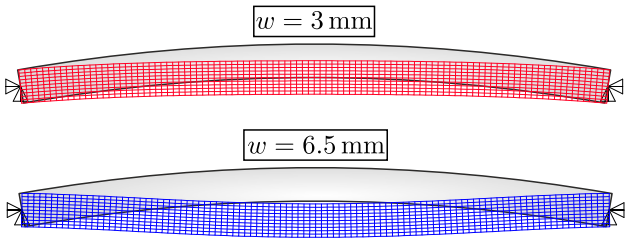

Fig. 20 Mean value of the deformed FE mesh for the displacement states $w = 3$ mm and $w = 6.5$ mm

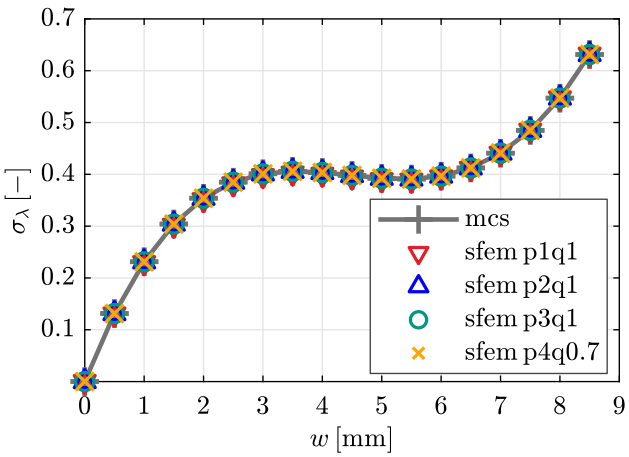

Fig. 21 Standard deviation σ_λ of the load factor λ for different combinations of the polynomial degree p and the q-norm q

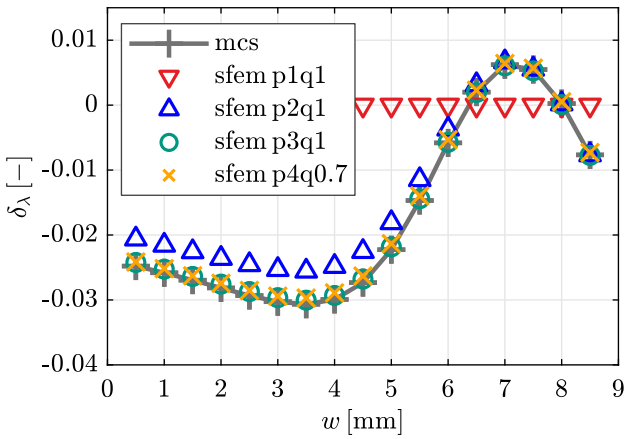

Fig. 22 Skewness δ_λ of the load factor λ for different combinations of the polynomial degree p and the q-norm q

seen that a linear polynomial basis with Hermite polynomials is insufficient to capture the skewness of a quantity that depends on normally distributed random variables.

The configuration sfem p2q1 increasingly approaches the reference solution from the MCS as the center displacement w increases. By using a cubic polynomial basis, the skewness δ_λ of the load factor is captured with high accuracy for the entire calculation. The skewness δ_λ obtained with the configuration sfem p4q0.7 is similar to that of sfem p3q1.

Table 4 Convergence behavior for the displacement step $w = 3\,\text{mm} \rightarrow 3.5\,\text{mm}$

No. of iter	sfem p2q1	sfem p3q1	sfem p4q0.7
1	1.066E−01	1.066E−01	1.066E−01
2	1.374E+00	1.374E+00	1.374E+00
3	1.965E−04	1.965E−04	1.965E−04
4	6.991E−11	6.980E−11	6.964E−11

Table 5 Speedup factor S_{sfem}: ratio between MCS and SSFEM computation time $T_{\text{mcs}}/T_{\text{sfem}}$

Settings	Notation	Speedup factor
$p = 1/q = 1$	sfem p1q1	2079.93
$p = 2/q = 1$	sfem p2q1	99.14
$p = 3/q = 1$	sfem p3q1	3.58
$p = 4/q = 0.7$	sfem p4q0.7	6.61

Table 4 shows the norm of the residual vector $\mathbf{G}$ during the Newton iteration for the displacement step $w = 3\,\text{mm} \rightarrow 3.5\,\text{mm}$. Due to the consistent linearization, all different SSFEM configurations show a quadratic convergence behavior near the equilibrium point. It should be noted that a similar convergence rate is observed for the configuration sfem p1q1, which is not shown.

Finally, it can be concluded that the iteration behavior is nearly independent of the chosen polynomial basis, and thus also of the polynomial degree p and the q-norm q.

7.2.2 Computational effort

As shown in Sect. 7.2.1, higher polynomial degrees are necessary to accurately capture stochastic moments such as the skewness. Table 3 illustrates that the number of degrees of freedom $ndof$ grows significantly with a higher polynomial degree. For a comparison of the computational effort, we consider the so-called speedup factor defined as

$$S_{\text{sfem}} = T_{\text{mcs}} \,/\, T_{\text{sfem}} \,, \tag{102}$$

where T_{mcs} and T_{sfem} are the computation times of the MCS and the SSFEM, respectively. Table 5 presents the speedup factors S_{sfem} of different SSFEM configurations compared to the MCS with 5×10^3 samples with reference to the computer environment used.

Within the Newton method, the current global stiffness matrix $\mathbf{K}_T$ must be factorized at each iteration step, see Eqs. (68) and (69). This process is decisive for the overall computation time. This can be seen in the significantly decreasing speedup factors S_{sfem} in Table 5. For the configuration sfem p4q0.7, which yields a good approximation

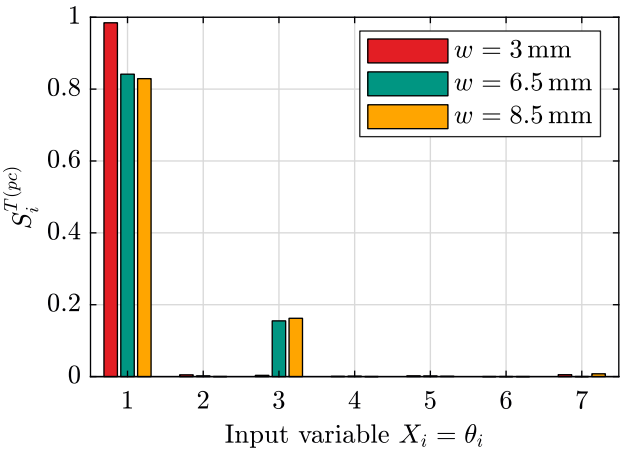

Fig. 23 Total PCE-based Sobol' indices $S_i^{T(pc)}$ for the three displacement levels $w = 3\,\text{mm}$, $w = 6.5\,\text{mm}$ and $w = 8.5\,\text{mm}$

quality up to the skewness, a speedup factor of 6.61 is obtained.

It should be noted that fewer MCS samples are required to approximate the mean value and the standard deviation, but also that a lower polynomial degree in the PC expansion is sufficient to capture these stochastic moments. However, the speedup factors in Table 5 can be scaled, e.g., if 5×10^2 MCS samples for the mean value would be sufficient, sfem p1q1 would result in a speedup factor of 207.99.

7.2.3 Sensitivity analysis

In the following, we investigate the sensitivity of the stochastic load factor λ with respect to the $M = 7$ input variables. Therefore, we consider the total PCE-based Sobol' indices at the three displacement levels $w = 3\,\text{mm}$, $w = 6.5\,\text{mm}$ and $w = 8.5\,\text{mm}$. These three displacement states are marked in Fig. 19. An advantage of the SSFEM is that the Sobol' indices are determined directly by post-processing an existing PC expansion. In our case, this corresponds to the PCE of the load factor λ, which is determined within the solution algorithm. The total Sobol' indices are evaluated based on the configuration sfem p4q0.7 and are illustrated in Fig. 23.

It is obvious, that the variability of the random load factor λ at the displacement step $w = 3\,\text{mm}$ is primarily influenced by the first input variable $X_1 = \theta_1$. At the displacement states $w = 6.5\,\text{mm}$ and $w = 8.5\,\text{mm}$, not only $X_1 = \theta_1$, but also $X_3 = \theta_3$ affects the variability of the load factor. The sensitivity index of the remaining input variables $X_i, i \in \{2, 4, 5, 6, 7\}$ is negligible, see Fig. 23.

Figure 24 depicts the first three eigenvalues $\lambda_i, i \in \{1, 2, 3\}$ and the corresponding eigenvectors $\boldsymbol{\varphi}_i, i \in \{1, 2, 3\}$.

The decreasing influence of the input variables $X_i, i = 1, \ldots, 7$ results from the decreasing magnitude of the eigenvalues $\lambda_i, i = 1, \ldots, 7$, as shown in Fig. 24. Furthermore,

the eigenvectors $\boldsymbol{\varphi}_i, i \in \{1, 3, 5, 7\}$ are symmetric, while the remaining eigenvectors $\boldsymbol{\varphi}_i, i \in \{2, 4, 6\}$ are asymmetric. This fact is also a reason for the different Sobol' indices $S_i^{T(pc)}$ of the input variables.

7.3 Single-hinged frame

The last example is a single-hinged frame under a stochastic line load $q_0(\omega)$, see Fig. 25. The geometry of the structure is inspired by the so-called Lee's frame [11]. A geometrically exact beam formulation is required to analyze the post-critical behavior of the structure, since both finite displacements and rotations occur.

A two-node Timoshenko beam element with linear shape functions is used for the spatial discretization of the structure. For the rectangular cross-section, the shear correction factor is $\kappa = 5/6$, see Fig. 25. The deterministic FE formulation of the underlying two-dimensional geometrically exact beam element can be found in e.g. [16, 24, 27]. To enable its application in the SSFEM, the deterministic element formulation has been appropriately extended to the stochastic setting. It should be noted that a co-rotational beam element with finite rotations within the SSFEM was proposed by [14].

The column has a height of 50 cm and is discretized into 20 elements. The beam has a length of 75 cm and is therefore divided into 30 elements. This spatial discretization results in a total of 50 elements and 51 nodal points.

The material behavior is isotropic and linear elastic. The Young's modulus of the structure is modeled as a spatially correlated Gaussian random field with the properties

$$E(\boldsymbol{x}, \omega) \sim \mathcal{N}(21000, 2100)\,\mathrm{kN/cm}^2\,. \tag{103}$$

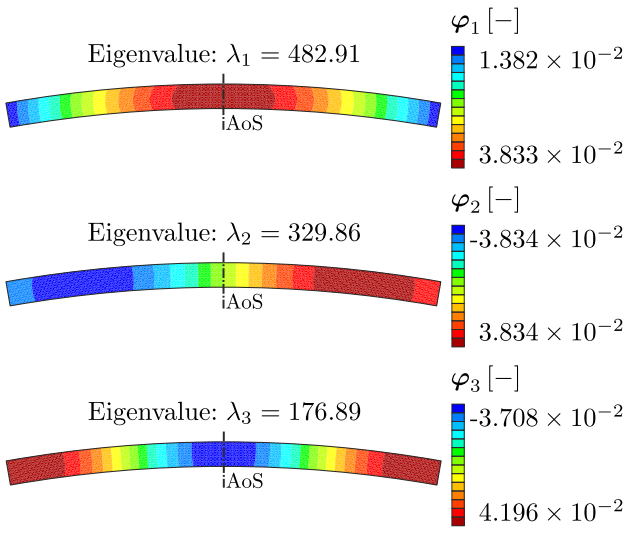

Fig. 24 First three eigenvalues $\lambda_i, i \in \{1, 2, 3\}$ and the corresponding eigenvectors $\boldsymbol{\varphi}_i, i \in \{1, 2, 3\}$

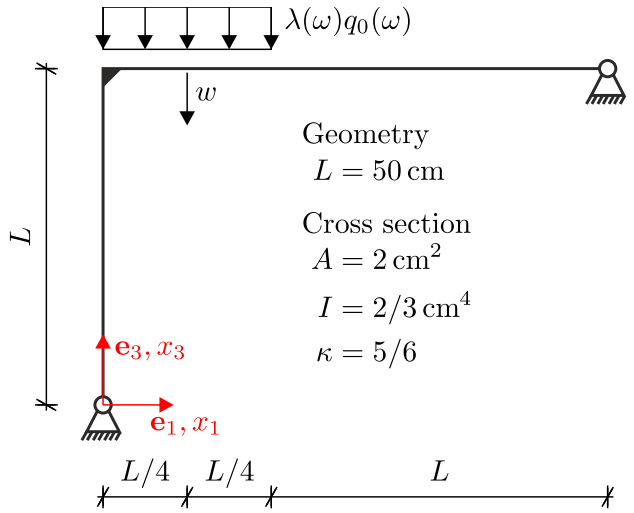

Fig. 25 Single-hinged frame: system, geometry, boundary conditions and external load

The Poisson's ratio of the material is $\nu = 0.3$. For the random field, we use the squared exponential correlation function, see Eq. (101), with a correlation length of $\ell_c = 30\,\mathrm{cm}$. With a quality measure of $Q = 0.99$, only six terms remain of the $N = 51$ terms in the KL expansion, see Eq. (106), where $N = 51$ corresponds to the total number of nodal points. The random field is constructed on a straight line with a total length of $50\,\mathrm{cm} + 75\,\mathrm{cm} = 125\,\mathrm{cm}$.

Additionally to the random Young's modulus, we consider the line load $q_0(\omega)$ as a Gaussian random variable with the properties

$$q_0(\omega) \sim \mathcal{N}(0.1, 0.01)\,\mathrm{kN/cm}\,. \tag{104}$$

Thus, a total of $M = 7$ normally distributed random variables are considered, summarized in the random vector

$$\begin{aligned}\mathbf{X}(\omega) &= [X_1,\ X_2,\ X_3,\ X_4,\ X_5,\ X_6,\ X_7]^T \\ &= [\theta_1,\ \theta_2,\ \theta_3,\ \theta_4,\ \theta_5,\ \theta_6,\ q_0]^T \in \mathbb{R}^7\,.\end{aligned} \tag{105}$$

For the approximation of the stochastic dimension, only Hermite polynomials are used.

The generalized displacement control from Sect. 5 is used to trace the equilibrium path. Within the solution algorithm, the displacement w is controlled, which is shown in Fig. 25. This displacement quantity is increased in steps of $\Delta w = 2\,\mathrm{cm}$ from 0 to 50 cm. Within the solution algorithm, the PC coefficients $\lambda_\alpha, \alpha \in \{0, \ldots, P\}$ associated with the stochastic line load $q_0(\omega)$ are calculated. It should be noted at this point that due to the line load, the application of the single displacement control, described in Sect. 4.2, is not possible.

Four different combinations of the polynomial degree p and the q-norm q are used for the computation with the

Table 6 Settings for SSFEM computation, notation, number of basis polynomials $\bar{P}$ and degrees of freedom $ndof \cdot \bar{P}$

Settings	Notation	$\bar{P}$	$ndof \cdot \bar{P}$
$p = 1/q = 1$	sfem p1q1	8	1192
$p = 2/q = 1$	sfem p2q1	36	5364
$p = 3/q = 0.8$	sfem p3q0.8	43	6407
$p = 4/q = 0.8$	sfem p4q0.8	127	18923

SSFEM. Table 6 shows all configurations of the SSFEM and the resulting number of degrees of freedom.

7.3.1 Results of the SSFEM

The results of the SSFEM configurations in Table 6 are compared with those of a Monte Carlo simulation. In order to get converged results with the MCS, a total of $N = 5 \times 10^5$ samples are used, similar to the previous example. The following figures depict the first three stochastic moments of the random load factor λ versus the deterministic controlled displacement w.

The mean value μ_λ of the load factor λ is shown in Fig. 26. For all SSFEM configurations, an excellent agreement with the MCS results is observed. Figure 26 additionally shows the mean value of the deformed structure for the two displacement states $w = 12\,\text{cm}$ and $w = 50\,\text{cm}$. It can be seen that large displacements and also large rotations already occur at the limit point at $w = 12\,\text{cm}$. This fact highlights the need for a geometrically exact beam formulation.

Figure 27 illustrates the standard deviation σ_λ of the load factor λ. A high agreement between the SSFEM and MCS results is observed. Minor deviations can only be recognized for the configuration sfem p1q1.

The skewness δ_λ is illustrated in Fig. 27. The approximation behavior of the SSFEM concerning the third stochastic moment is similar to that of the previous numerical examples in Sects. 7.1 and 7.2. Using the configuration sfem p4q0.8, the skewness of the load factor is captured with high accuracy throughout the entire computation.

In Appendix E, we provide further investigations of the stochastic load factor λ at the displacement level $w = 28\,\text{cm}$. In addition to the convergence behavior of the MCS with respect to the number of samples, we also examine the approximation quality of the SSFEM results.

In order to visualize the variation of the stochastic load factor, Fig. 29 illustrates the mean value μ_λ plus minus three times the standard deviation σ_λ. In addition, this graph shows multiple random load displacement curves. This diagram clearly illustrates the influence of the random modeling of the Young's modulus $E(\boldsymbol{x}, \omega)$ and the line load $q_0(\omega)$ on the structural behavior of the frame.

Table 7 Convergence behavior for the displacement step $w = 12\,\text{cm} \rightarrow 14\,\text{cm}$

No. of iter	sfem p2q1	sfem p3q0.8	sfem p4q0.8
1	7.744E−01	7.744E−01	7.744E−01
2	3.447E+02	3.448E+02	3.447E+02
3	4.675E+00	4.647E+00	4.652E+00
4	8.312E−01	8.403E−01	8.385E−01
5	3.268E−02	3.224E−02	3.277E−02
6	1.732E−04	1.625E−04	1.821E−04
7	3.827E−09	2.396E−09	4.218E−09

Furthermore, Fig. 30 depicts the mean value plus minus three times the standard deviation of the deformed structure at three different displacement states. The highlighted nodal point in each deformed mesh is the node at which the displacement w is prescribed within the solution algorithm. Since this displacement quantity is deterministic, all marked points for one displacement state are located on a horizontal line. Due to the uncertainties of the Young's modulus and the line load $q_0(\omega)$, all remaining nodal displacements are stochastic quantities.

Similar to the previous examples, the convergence behavior of the stochastic element formulation within the Newton iteration is investigated. Therefore, we consider the displacement step $w = 12\,\text{cm} \rightarrow 14\,\text{cm}$, see Fig. 26. The norm of the global residual vector $\mathbf{G}$ is shown in Table 7.

It is obvious that for the different configurations of the SSFEM, a quadratic convergence behavior is achieved in the vicinity of the equilibrium point. A similar convergence rate is observed for the configuration sfem p1q1, which is not shown.

7.3.2 Computational effort

For a comparison of the computational effort, we consider the computation times of the MCS and the SSFEM. Table 8 illustrates the speedup factors of different SSFEM configurations compared to the MCS with 5×10^3 samples.

Similar to the second numerical example in Sect. 7.2, the computation time for the SSFEM depends significantly on the polynomial degree of the underlying PC expansion. With increasing degrees of freedom $ndof$, the speedup factors decrease significantly. The configuration sfem p4q0.8 is 2.08 times faster than the MCS with 5×10^3 samples and provides an excellent approximation up to the skewness. As described in Sect. 7.2.2, the speedup factors in Table 8 can be scaled.

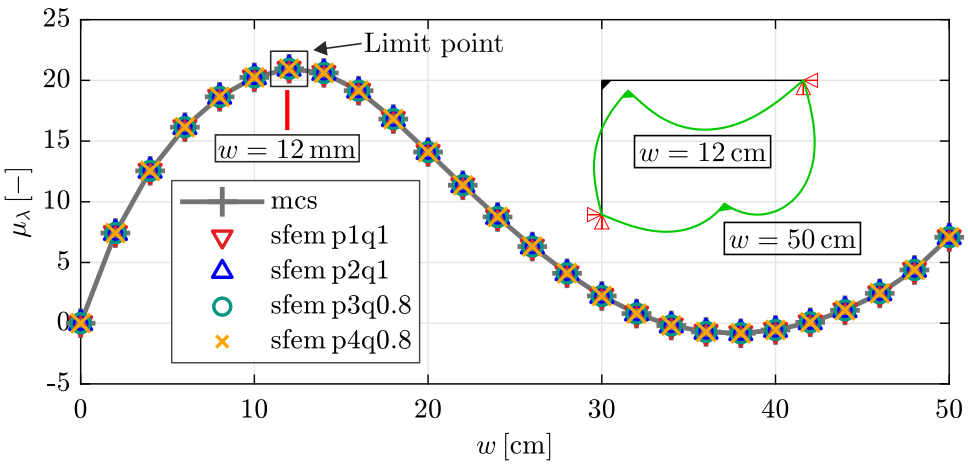

Fig. 26 Mean value μ_λ of the load factor λ for different combinations of the polynomial degree p and the q-norm q

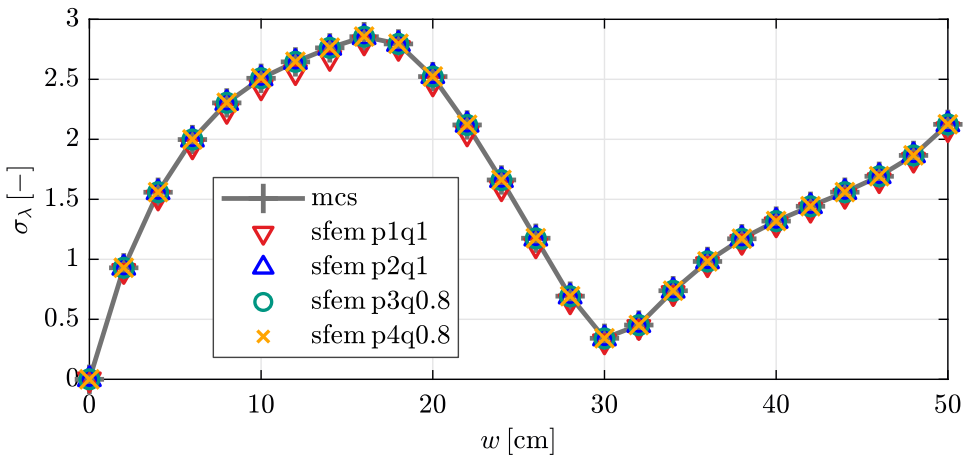

Fig. 27 Standard deviation σ_λ of the load factor λ for different combinations of the polynomial degree p and the q-norm q

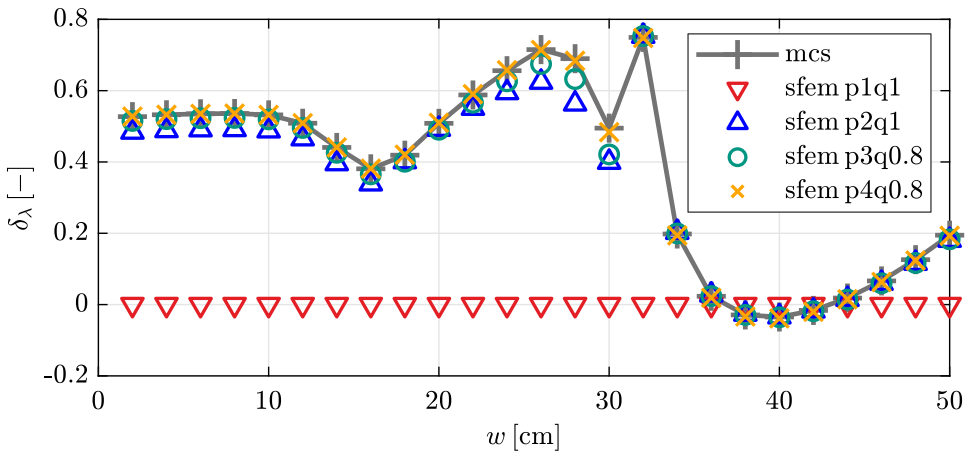

Fig. 28 Skewness δ_λ of the load factor λ for different combinations of the polynomial degree p and the q-norm q

7.3.3 Probability density function

Finally, the probability density function (PDF) $f_\lambda(\lambda|w = 28\,\text{cm})$ of the load factor λ at the displacement state $w = 28\,\text{cm}$ is examined in more detail. The estimation of the probability density function is performed in the same way as described in Sect. 7.1.3.

A set of $N = 5 \times 10^5$ realizations of the random vector $\mathbf{X}(\omega)$ in Eq. (105) is used to perform an MCS with both the full FE model and the surrogate model provided by the SSFEM calculation. The reference solution obtained using the FE model is labeled mcs + fem.

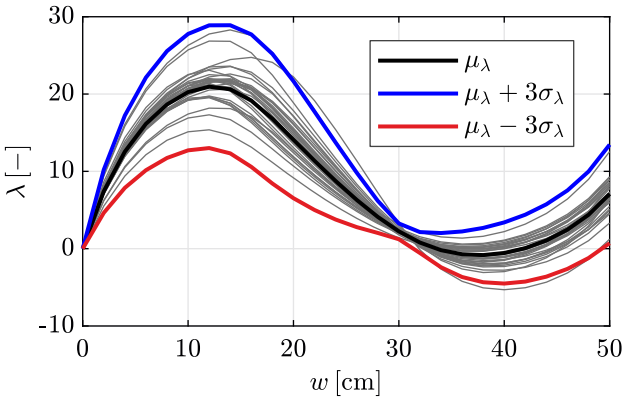

Fig. 29 Mean value μ_λ plus minus three times the standard deviation σ_λ as well as random realizations of the load–displacement curves

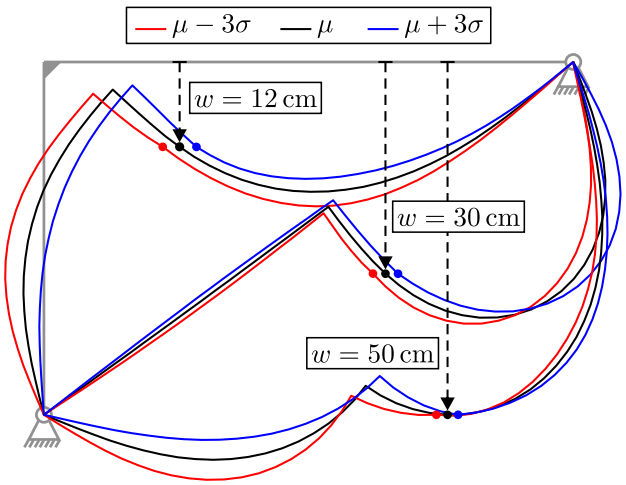

Fig. 30 Mean value plus minus three times the standard deviation of the deformed structure for three different displacement states

Table 8 Speedup factor S_{sfem}: ratio between MCS and SSFEM computation time $T_{\text{mcs}}/T_{\text{sfem}}$

Notation	Notation	Speedup factor
$p = 1/q = 1$	sfem p1q1	1615.82
$p = 2/q = 1$	sfem p2q1	191.07
$p = 3/q = 0.8$	sfem p3q0.8	48.04
$p = 4/q = 0.8$	sfem p4q0.8	2.08

The results of the estimated probability density function are shown in Fig. 31.

As already shown in Fig. 28, sfem p1pq1 is not able to capture the skewness of the load factor λ. The insufficient approximation between the random vector $\mathbf{X}(\omega)$ and the load factor λ is also evident in the PDF, see Fig. 31 (top). As shown in Fig. 31 (bottom), a higher polynomial degree leads to a very accurate approximation of the estimated probability density function.

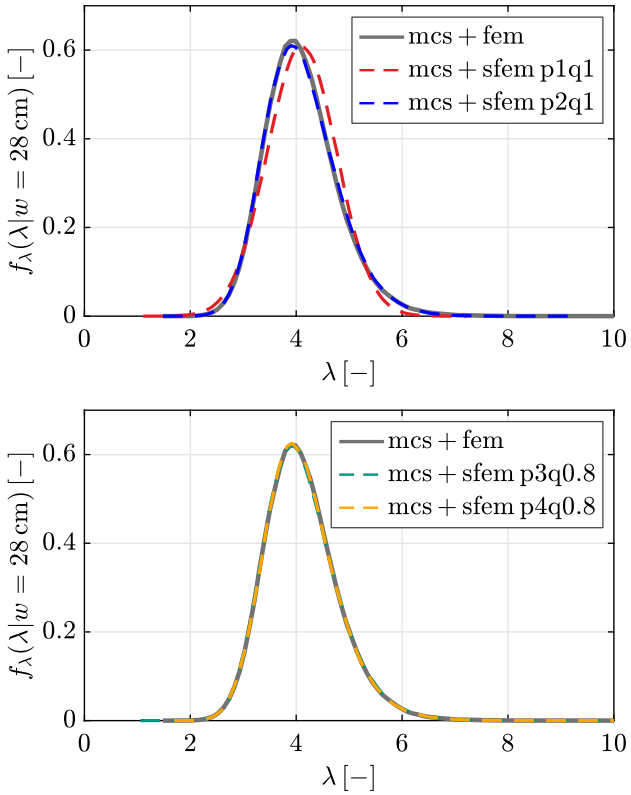

Fig. 31 Probability density function (PDF) $f_\lambda(\lambda|w = 28\,\text{cm})$ of the load factor λ at the displacement level $w = 28$ cm

8 Conclusion and outlook

In the present paper, a new solution algorithm, referred to as generalized displacement control, has been proposed to trace the equilibrium path of geometrically nonlinear structures within the framework of the SSFEM. In this solution procedure, a user-defined displacement quantity is prescribed. The corresponding load factor for the external load is computed instead of a reaction force, thereby removing restrictions on the type of the external load. The key idea is to extend the global residual vector by an additional set of constraint equations, leading to an extended system of nonlinear equations. To solve this system within a Newton iteration scheme, all equations are consistently linearized. Subsequently, the proposed algorithm is validated using three numerical examples that confirm its accuracy, robustness, and applicability for nonlinear spectral stochastic finite element analysis.

We investigated the geometrically nonlinear behavior of various structures subjected to uncertain material and geometrical properties as well as random external loads. The examined structures include a cylindrical shell, an arch structure, and a single-hinged frame. Within the SSFEM, all stochastic quantities are characterized by their individual PC coefficients. Therefore, the stochastic moments are determined directly by post-processing an existing PC expansion.

For all numerical examples, the results of the SSFEM and the MCS show excellent agreement. The studies demonstrate that the size of the polynomial basis, which depends on the polynomial degree p and the q-norm q, has a significant influence on the accuracy of the SSFEM results. In addition, Sobol' indices can be determined directly within a post-processing procedure. The investigations show that the variability of a quantity of interest is affected to varying degrees by the individual input variables. Furthermore, the surrogate model obtained from the SSFEM has been used together with the MCS in a post-processing step to compute the probability density function of a quantity of interest. The numerical examples demonstrate excellent agreement between the MCS using the surrogate model and the full FE model.

Despite the advantages of the SSFEM, the method also has certain limitations, particularly for large problems with high stochastic dimensions. The exponential growth of the polynomial basis leads to large systems of equations that must be solved in each iteration step. In this paper, only direct solvers have been used. However, they can become impractical when solving such large systems of equations. To address these challenges, iterative solver techniques can be employed, but they require appropriate preconditioning to achieve reliable and efficient convergence.

The proposed solution algorithm allows the calculation of problems that cannot be investigated with standard solution algorithms within the framework of the SSFEM. This includes the snap-through behavior of the arch structure and the single-hinged frame. In all numerical examples, the proposed generalized displacement control exhibits quadratic convergence near an equilibrium point due to the consistent linearization of all equations.

Future research will focus on further mixed element formulations based on Hu–Washizu functionals. In addition, the development of a general path-following algorithm, such as the arc-length method, within the framework of the SSFEM will be part of future work.

A Random fields and PC approximation

We consider a spatially correlated Gaussian random field $H(\boldsymbol{x}, \omega)$, which is discretized using the Karhunen–Loève expansion (KLE)

$$H(\boldsymbol{x}, \omega) \approx \widehat{H}(\boldsymbol{x}, \omega) = \mu_H + \sum_{i=1}^{N} \theta_i(\omega) \sqrt{\lambda_i}\, \boldsymbol{\varphi}_i(\boldsymbol{x}) \,, \quad (106)$$

where $\theta_i(\omega) \sim \mathcal{N}(0, 1)$ is a standard normal distribution. Furthermore, λ_i and $\boldsymbol{\varphi}_i(\boldsymbol{x})$ are the i-th eigenvalue and eigenvector of the covariance matrix

$$\boldsymbol{C} = \sigma_H^2 \begin{bmatrix} \rho(\boldsymbol{x}_1, \boldsymbol{x}_1) & \dots & \rho(\boldsymbol{x}_1, \boldsymbol{x}_N) \\ \vdots & \rho(\boldsymbol{x}_i, \boldsymbol{x}_k) & \vdots \\ \rho(\boldsymbol{x}_N, \boldsymbol{x}_1) & \dots & \rho(\boldsymbol{x}_N, \boldsymbol{x}_N) \end{bmatrix} \in \mathbb{R}^{N \times N} \,, \quad (107)$$

where $\rho(\boldsymbol{x}_i, \boldsymbol{x}_k)$ denotes a correlation function and N is the number of discrete spatial points $\boldsymbol{x}$. Since we assume a stationary random field, the mean value μ_H and the variance σ_H^2 are constant over the spatial domain.

For smooth random fields, the magnitude of the eigenvalues λ_i decreases rapidly and therefore the N terms in Eq. (106) can be reduced to $K \leq N$. Thus, the quality measure Q is introduced

$$Q = \Big(\sum_{i=1}^{K} \lambda_i\Big) \,/\, \Big(\sum_{i=1}^{N} \lambda_i\Big) \,. \quad (108)$$

In general, a value of $Q = 0.99$ is sufficient to considerably reduce the number of KLE terms, and consequently, the number of random input variables for a PC expansion.

In the context of the SSFEM, an explicit representation of the discretized random field $\widehat{H}(\boldsymbol{x}, \omega)$ with the PCE is necessary. Therefore, we introduce the PC expansion

$$\widehat{H}(\boldsymbol{x}, \omega) = \widehat{H}^{pc}(\boldsymbol{x}, \omega) = \sum_{\alpha=0}^{K} h_\alpha(\boldsymbol{x})\, \Psi_\alpha(\boldsymbol{\theta}) \,, \quad (109)$$

where the K standard normal distributed random variables are arranged in the random vector $\boldsymbol{\theta} = [\theta_1, \dots, \theta_K]^T$. Furthermore, $\Psi_\alpha(\boldsymbol{\theta})$ and $h_\alpha(\boldsymbol{x})$ denote the multivariate Hermite polynomials and the spatially varying PC coefficients, respectively. For clarity, the random variables are denoted by Θ throughout this section to avoid any confusion with the spatial coordinates $\boldsymbol{x}$. The coefficients $h_\alpha(\boldsymbol{x})$ are determined by an orthogonal projection. Due to the orthonormality condition of the basis polynomials, see Eq. (5), the PC coefficients are given by

$$\begin{aligned} h_0(\boldsymbol{x}) &= \mathbb{E}\big[\widehat{H}(\boldsymbol{x}, \omega)\Psi_0(\boldsymbol{\Theta})\big] \\ &= \int_{D_{\boldsymbol{\Theta}}} \widehat{H}(\boldsymbol{x}, \omega) \underbrace{\Psi_0(\boldsymbol{\theta})}_{=1} f_{\boldsymbol{\Theta}}(\boldsymbol{\theta})\, \mathrm{d}\boldsymbol{\theta} = \mu_H \end{aligned} \quad (110)$$

and

$$\begin{aligned} h_\alpha(\boldsymbol{x}) &= \mathbb{E}\big[\widehat{H}(\boldsymbol{x}, \omega)\Psi_\alpha(\boldsymbol{\Theta})\big] \\ &= \int_{D_{\boldsymbol{\Theta}}} \widehat{H}(\boldsymbol{x}, \omega)\Psi_\alpha(\boldsymbol{\theta})\, f_{\boldsymbol{\Theta}}(\boldsymbol{\theta})\, \mathrm{d}\boldsymbol{\theta} = \sqrt{\lambda_\alpha}\, \boldsymbol{\varphi}_\alpha(\boldsymbol{x}) \,, \end{aligned} \quad (111)$$

where $\alpha = 1, \ldots, K$. Since the random variables $\Theta_i(\omega)$, $i = 1, \ldots, K$ are linear in the KLE in Eq. (106), the discretized random field is represented exactly with a linear PC expansion. Thus, the projections on all higher-order basis polynomials with $\alpha > K$ are equal to zero.

B Vectorized implementation of arithmetic operations with PC expansions

Various arithmetic operations with PC expansions are essential components of stochastic FE formulations and solution algorithms, as described in the present paper. This appendix provides several algorithms that can be used for an efficient implementation of the SSFEM, e.g., in MATLAB [23].

For implementation purposes, it is reasonable to store the components of the multiplication tensor $D_{\alpha\beta\gamma}$ as a matrix. Therefore, we define the quantity

$$\boldsymbol{D}_\alpha := \begin{bmatrix} D_{\alpha 00} & \ldots & D_{\alpha 0 P} \\ \vdots & D_{\alpha\beta\gamma} & \vdots \\ D_{\alpha P 0} & \ldots & D_{\alpha P P} \end{bmatrix} \in \mathbb{R}^{\bar{P}\times\bar{P}} \,, \quad \alpha \in \{0, \ldots, P\} \,. \tag{112}$$

This allows the elements of the multiplication tensor to be arranged into the matrix

$$\mathbf{M} := \big[\mathrm{vec}\,(\boldsymbol{D}_0), \ldots, \underbrace{\mathrm{vec}\,(\boldsymbol{D}_\alpha)}_{\mathbf{M}(:,\alpha+1)}, \ldots, \mathrm{vec}\,(\boldsymbol{D}_P)\big] \,, \tag{113}$$

where $\mathbf{M} \in \mathbb{R}^{\bar{P}^2\times\bar{P}}$. The expression $\mathrm{vec}\,(\boldsymbol{D}_\alpha)$ denotes the vectorization of the matrix $\boldsymbol{D}_\alpha$. Thereby, the matrix $\boldsymbol{D}_\alpha$ is transformed column by column into a vector, which is then arranged in the $(\alpha+1)$-th column of the matrix $\mathbf{M}$. Following the notation in MATLAB [23], this column is denoted by $\mathbf{M}(:, \alpha+1)$. Since only a small number of elements in $\mathbf{M}$ are non-zero, it can be efficiently stored as a sparse matrix.

In the context of the implementation, PC variables are defined as row vectors. The $\bar{P}$ coefficients of the two known PC expansions are stored in the vectors

$$\mathbf{b} = [b_0, \ldots, b_P] \in \mathbb{R}^{1\times\bar{P}} \,, \quad \mathbf{c} = [c_0, \ldots, c_P] \in \mathbb{R}^{1\times\bar{P}} \,. \tag{114}$$

Furthermore,

$$\mathbf{a} = [a_0, \ldots, a_P] \in \mathbb{R}^{1\times\bar{P}} \tag{115}$$

contains the unknown PC coefficients.

Algorithm 4 illustrates the multiplication $\mathbf{a} = \mathbf{b} \cdot \mathbf{c}$ of the two PC expansions in Eq. (114).

Algorithm 4 Multiplication $\mathbf{a} = \mathbf{b} \cdot \mathbf{c}$

Input: $\mathbf{b} \in \mathbb{R}^{1\times\bar{P}}$, $\mathbf{c} \in \mathbb{R}^{1\times\bar{P}}$, $\mathbf{M} \in \mathbb{R}^{\bar{P}^2\times\bar{P}}$
Output: $\mathbf{a} \in \mathbb{R}^{1\times\bar{P}}$
function [**a**] = PCmul(**b**, **c**, **M**)
  $\mathbf{S} = \mathbf{b} \otimes \mathbf{c}$, $\mathbf{S} \in \mathbb{R}^{\bar{P}\times\bar{P}}$ ▷ Dyadic product
  $\mathbf{s} = \mathrm{vec}(\mathbf{S})$, $\mathbf{s} \in \mathbb{R}^{\bar{P}^2\times 1}$ ▷ Reshape matrix to vector
  $\mathbf{a} = \mathbf{s}^T\mathbf{M}$
end

An illustrative example of the multiplication of two PC expansions is given in Appendix C of [13].

The procedure for the division $\mathbf{a} = \mathbf{c}/\mathbf{b}$ is shown in Algorithm 5.

Algorithm 5 Division $\mathbf{a} = \mathbf{c}/\mathbf{b}$

Input: $\mathbf{c} \in \mathbb{R}^{1\times\bar{P}}$, $\mathbf{b} \in \mathbb{R}^{1\times\bar{P}}$, $\mathbf{M} \in \mathbb{R}^{\bar{P}^2\times\bar{P}}$
Output: $\mathbf{a} \in \mathbb{R}^{1\times\bar{P}}$
function [**a**] = PCdiv(**c**, **b**, **M**)
  $\bar{\mathbf{b}} = \mathbf{b}^T\mathbf{M}$, $\bar{\mathbf{b}} \in \mathbb{R}^{\bar{P}^2\times 1}$
  $\mathbf{B} = \mathrm{vec}^{-1}_{\bar{P},\bar{P}}(\bar{\mathbf{b}})$, $\mathbf{B} \in \mathbb{R}^{\bar{P}\times\bar{P}}$ ▷ Reshape vector to matrix
  $\mathbf{a} = \mathbf{c}\,\mathbf{B}^{-1}$ ▷ Solve system of equations
end

The expression $\mathrm{vec}^{-1}_{\bar{P},\bar{P}}(\bullet)$ denotes the inverse operation of the column-wise vectorization $\mathrm{vec}(\bullet)$ mentioned before. In the operation $\mathbf{B} = \mathrm{vec}^{-1}_{\bar{P},\bar{P}}(\bar{\mathbf{b}})$, the vector $\bar{\mathbf{b}} \in \mathbb{R}^{\bar{P}^2\times 1}$ is reshaped into the matrix $\mathbf{B} \in \mathbb{R}^{\bar{P}\times\bar{P}}$.

Another important arithmetic operation in the SSFEM is the augmentation of a PC expansion, see Eqs. (21) and (60). We consider the PC expansion of the stochastic matrix

$$\mathbf{D}(\omega) = \sum_{\alpha=0}^{P} \mathbf{D}_\alpha \Psi_\alpha \quad \text{with} \quad \mathbf{D}_\alpha \in \mathbb{R}^{nr\times nc} \,, \tag{116}$$

where nr and nc denote the number of rows and columns, respectively. All PC coefficients are arranged in an augmented matrix $\mathbf{D} \in \mathbb{R}^{(nr\cdot\bar{P})\times(nc\cdot\bar{P})}$, see Eq. (63). For the implementation the components $\mathbf{D}_\alpha$ are arranged in the matrix

$$\mathbf{d} = \big[\mathrm{vec}\,(\mathbf{D}_0), \ldots, \mathrm{vec}\,(\mathbf{D}_\alpha), \ldots, \mathrm{vec}\,(\mathbf{D}_P)\big] \,, \tag{117}$$

where $\mathbf{d} \in \mathbb{R}^{(nr\cdot nc)\times\bar{P}}$. The matrix $\mathbf{D}$ is then derived from the array $\mathbf{d}$ in Eq. (117). An efficient implementation of this augmentation is shown in Algorithm 6.

Algorithm 6 Augmentation $\mathbf{D}_{\alpha\beta} = D_{\alpha\beta\gamma}\mathbf{D}_{\gamma}$

Input: $\mathbf{d} \in \mathbb{R}^{(nr\cdot nc)\times \bar{P}}$, nr, nc, $\mathbf{M} \in \mathbb{R}^{\bar{P}^2\times \bar{P}}$
Output: $\mathbf{D} \in \mathbb{R}^{(nr\cdot \bar{P})\times(nc\cdot \bar{P})}$
function [**D**] = PCaug(**d**, nr, nc, **M**)
  $\bar{\mathbf{d}} = \mathbf{d}\,\mathbf{M}^T$ ▷ Multiplication with multiplication tensor
  $\mathbf{ir} = [1,\ldots,nr] \in \mathbb{R}^{\bar{P}}$, $\mathbf{ic} = [1,\ldots,nc] \in \mathbb{R}^{\bar{P}}$
  for $j = 1,\ldots,nr$ **do**
    $\mathbf{ii} = \mathbf{ir} + nr\cdot(j-1)$ ▷ Pointer for rows
    for $k = 1,\ldots,nc$ **do**
      $\mathbf{kk} = \mathbf{ic} + nc\cdot(k-1)$ ▷ Pointer for columns
      ip $= k + \bar{P}\cdot(i-1)$ ▷ Linear column index
      $\mathbf{D}(\mathbf{ii},\mathbf{kk}) = \mathrm{vec}^{-1}_{nr\times nc}\left(\bar{\mathbf{d}}(:,\mathrm{ip})\right)$ ▷ Assembly
    end for
  end for
end

C Element framework for a geometrically nonlinear spectral stochastic solid element

In order to provide a comprehensive understanding of the SSFEM, the following section presents all algorithms required for an efficient implementation of a stochastic FE formulation, e.g., in MATLAB [23]. The spectral stochastic formulation presented here refers to a two-dimensional continuum element. For a classical FE formulation of such an element, the reader is referred to [27].

The stochastic displacement field is $\mathbf{u}(\omega) = [u_1, u_2]^T$, see Fig. 32. Assuming a plane stress state, the relevant components of the stochastic Green-Lagrangian strain tensor and the 2^{nd} Piola-Kirchhoff stress tensor are given by

$$\mathbf{E}(\omega) = [E_{11},\ E_{22},\ 2E_{12}]^T,\ \mathbf{S}(\omega) = [S_{11},\ S_{22},\ S_{12}]^T\ . \tag{118}$$

Furthermore, the necessary components of the stochastic displacement gradient $\mathbf{H}(\omega)$ are arranged in the column vector

$$\mathbf{h}(\omega) = [u_{1,1},\ u_{1,2},\ u_{2,1},\ u_{2,2}]^T\ . \tag{119}$$

For linear elastic, isotropic materials, the stochastic material matrix reads

$$\mathbf{C}(\omega) = \frac{Ed}{1-\nu^2}\begin{bmatrix} 1 & \nu & 0 \\ \nu & 1 & 0 \\ 0 & 0 & (1-\nu)/2 \end{bmatrix}, \tag{120}$$

where E is the Young's modulus, ν the Poisson's ratio and d the thickness, see Fig. 32.

For the spatial discretization, quadrilateral elements with $nel = 4$ are used. The displacement vector of node I, associated with the polynomial Ψ_α, is denoted by $\mathbf{v}_{I\alpha} = [u_{1\alpha}, u_{2\alpha}]^T$, as depicted in Fig. 32.

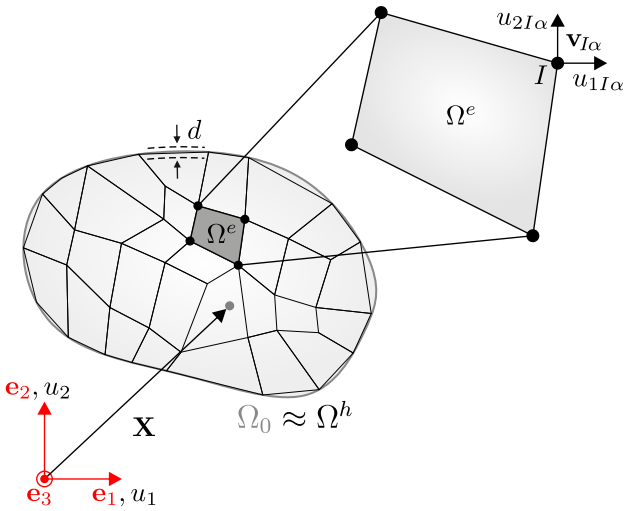

Fig. 32 Spatial discretization with quadrilateral elements

The general framework for calculating the residual vector $\mathbf{g}^e$ and the corresponding tangent stiffness matrix $\mathbf{k}^e_T$, described in Sect. 6.2, is shown in Algorithm 7.

Algorithm 7 Element framework for a spectral stochastic formulation

for $ig = 1,\ldots,ngp$ **do** ▷ Loop integration points
  [**N**, det **J**] = Shape($\mathbf{x}_{gp}$)
  h = Grad(**v**, **N**)
  E = Eps(**h**, **M**)
  [**S**, **C**] = Mate(**E**, **M**)
  for $I = 1,\ldots,nel$ **do** ▷ Loop node I
    $\mathbf{B}_I$ = Bmat(**h**, **M**, **N**)
    $\mathbf{f}_I$ = Fint($\mathbf{B}_I$, **S**, det **J**, w_{gp})
    $\mathbf{g}^e \leftarrow \mathbf{g}^e + \mathbf{f}_I$ ▷ Element residual vector
    for $K = 1,\ldots,nel$ **do** ▷ Loop node K
      $\mathbf{B}_K$ = Bmat(**h**, **M**, **N**)
      $\mathbf{k}_{TIK}$ = Tang($\mathbf{B}_I$, $\mathbf{B}_K$, **C**, **S**, **N**, **M**, det **J**, w_{gp})
      $\mathbf{k}^e_T \leftarrow \mathbf{k}^e_T + \mathbf{k}_{TIK}$ ▷ Element tangent stiffness matrix
    end for
  end for
end for

It is obvious that the structure of the element routine is the same as in a classical FE formulation. The numerical integration is carried out using $ngp = 4$ Gauss-Legendre integration points. Within the individual routines, some differences are recognizable, as special arithmetic operations with PC variables have to be performed as part or the stochastic formulation.

Within Algorithm 8 the Cartesian derivatives of the bilinear shape functions and the determinant of the Jacobian matrix **J** are evaluated at the current integration point.

Algorithm 8 Shape functions

Input: $\mathbf{x}_{gp} \in \mathbb{R}^{1\times 2}$

Output: $\mathbf{N} \in \mathbb{R}^{2\times 4}$, $\det \mathbf{J}$

function $[\mathbf{N}, \det \mathbf{J}] = \text{Shape}(\mathbf{x}_{gp})$

$$\mathbf{N} = \begin{bmatrix} N_{1,1} & \dots & N_{I,1} & \dots & N_{4,1} \\ N_{1,2} & \dots & N_{I,2} & \dots & N_{4,2} \end{bmatrix}, \quad \det \mathbf{J} = \det \begin{bmatrix} X_{1,\xi} & X_{1,\eta} \\ X_{2,\xi} & X_{2,\eta} \end{bmatrix}$$

end

The PC coefficients of the stochastic displacement gradients are computed in Algorithm 9. At this point, it should be noted again that within the implementation the individual PC coefficients of different stochastic quantities are stored column-wise, see $\mathbf{h} \in \mathbb{R}^{4\times \bar{P}}$. The PC expansions of the four independent components of the stochastic displacement gradient are stored row by row, where the ordering corresponds to that in Eq. (119).

Algorithm 9 Displacement gradients

Input: $\mathbf{v} \in \mathbb{R}^{8\bar{P}\times 1}$, $\mathbf{N} \in \mathbb{R}^{2\times 4}$

Output: $\mathbf{h} \in \mathbb{R}^{4\times \bar{P}}$

function $[\mathbf{h}] = \text{Grad}(\mathbf{v}, \mathbf{N})$

$$\bar{\mathbf{v}} := \begin{bmatrix} \mathbf{v}_{10} & \dots & \mathbf{v}_{40} \\ \vdots & \mathbf{v}_{I\alpha} & \vdots \\ \mathbf{v}_{1P} & \dots & \mathbf{v}_{4P} \end{bmatrix} \in \mathbb{R}^{2\bar{P}\times 4}, \quad \mathbf{h} = \begin{bmatrix} \mathbf{h}_1 \\ \mathbf{h}_2 \\ \mathbf{h}_3 \\ \mathbf{h}_4 \end{bmatrix} =$$

$\text{reshape}(\mathbf{N}\bar{\mathbf{v}}^T, 4, \bar{P})$

end

Based on the displacement gradient coefficients, the PC expansions of the nonlinear strain components are computed, see Algorithm 10. First, the multiplication routine from Algorithm 4 is used to compute the nonlinear strain terms. Therefore, the multiplication tensor $\mathbf{M} \in \mathbb{R}^{\bar{P}^2\times \bar{P}}$, defined in Eq. (113), is required.

Algorithm 10 Strains

Input: $\mathbf{h} \in \mathbb{R}^{4\times \bar{P}}$, $\mathbf{M} \in \mathbb{R}^{\bar{P}^2\times \bar{P}}$

Output: $\mathbf{E} \in \mathbb{R}^{3\bar{P}\times 1}$

function $[\mathbf{E}] = \text{Eps}(\mathbf{h}, \mathbf{M})$

$\mathbf{h}_1^2 = \text{PCmul}(\mathbf{h}_1, \mathbf{h}_1, \mathbf{M})$, $\mathbf{h}_2^2 = \text{PCmul}(\mathbf{h}_2, \mathbf{h}_2, \mathbf{M})$

$\mathbf{h}_3^2 = \text{PCmul}(\mathbf{h}_3, \mathbf{h}_3, \mathbf{M})$, $\mathbf{h}_4^2 = \text{PCmul}(\mathbf{h}_4, \mathbf{h}_4, \mathbf{M})$

$\mathbf{h}_{12} = \text{PCmul}(\mathbf{h}_1, \mathbf{h}_2, \mathbf{M})$, $\mathbf{h}_{34} = \text{PCmul}(\mathbf{h}_3, \mathbf{h}_4, \mathbf{M})$

$$\mathbf{e} = \begin{bmatrix} \mathbf{e}_1 \\ \mathbf{e}_2 \\ \mathbf{e}_3 \end{bmatrix} = \begin{bmatrix} \mathbf{h}_1 + (\mathbf{h}_1^2 + \mathbf{h}_3^2)/2 \\ \mathbf{h}_4 + (\mathbf{h}_2^2 + \mathbf{h}_4^2)/2 \\ \mathbf{h}_2 + \mathbf{h}_3 + \mathbf{h}_{12} + \mathbf{h}_{34} \end{bmatrix} \in \mathbb{R}^{3\times \bar{P}}$$

$\mathbf{E} = \text{vec}(\mathbf{e})$

end

Subsequently, the augmented material matrix $\mathbf{C} \in \mathbb{R}^{3\bar{P}\times 3\bar{P}}$ is computed. To this end, the PC coefficients of all nine stiffness components are defined and then arranged in the matrix $\mathbf{c} \in \mathbb{R}^{9\times \bar{P}}$. An illustrative example of how to calculate the PC coefficients of a material matrix can be found in [13] Appendix E. Using the routine in Algorithm 6, the matrix $\mathbf{C}$ is computed. Together with the strains $\mathbf{E} \in \mathbb{R}^{3\bar{P}\times 1}$, all PC coefficients of the stresses $\mathbf{S} \in \mathbb{R}^{3\bar{P}\times 1}$ are obtained.

Algorithm 11 Material law

Input: $\mathbf{E} \in \mathbb{R}^{3\bar{P}\times 1}$, $\mathbf{M} \in \mathbb{R}^{\bar{P}^2\times \bar{P}}$

Output: $\mathbf{S} \in \mathbb{R}^{3\bar{P}\times 1}$, $\mathbf{C} \in \mathbb{R}^{3\bar{P}\times 3\bar{P}}$

function $[\mathbf{S}, \mathbf{C}] = \text{Mate}(\mathbf{E}, \mathbf{M})$

$$\mathbf{c} = \begin{bmatrix} \mathbf{c}_1 \\ \vdots \\ \mathbf{c}_9 \end{bmatrix} \in \mathbb{R}^{9\times \bar{P}}$$ ▷ set PC coefficients of material matrix

$\mathbf{C} = \text{PCaug}(\mathbf{c}, 3, 3, \mathbf{M})$

$\mathbf{S} = \mathbf{C}\,\mathbf{E}$

end

The vector of internal forces is calculated within the first loop over all nodes, indicated by I. For this purpose, the B-matrix $\mathbf{B}_I \in \mathbb{R}^{3\bar{P}\times 2\bar{P}}$ for node I is computed in Algorithm 12. The procedure for calculating the augmented matrix $\mathbf{B}_I$ is similar to that for the material matrix $\mathbf{C}$. At this point, it should be noted that the PC expansion of a constant quantity is only non-zero on the first PC coefficient, see variable $\bar{\mathbf{1}}$.

Algorithm 12 B-matrix

Input: $\mathbf{h} \in \mathbb{R}^{4\times \bar{P}}$, $\mathbf{M} \in \mathbb{R}^{\bar{P}^2\times \bar{P}}$, $\mathbf{N} \in \mathbb{R}^{2\times 4}$

Output: $\mathbf{B}_I \in \mathbb{R}^{3\bar{P}\times 2\bar{P}}$

function $[\mathbf{B}_I] = \text{Bmat}(\mathbf{h}, \mathbf{M}, \mathbf{N})$

$\bar{\mathbf{1}} = [1, 0, \dots, 0, \dots, 0] \in \mathbb{R}^{1\times \bar{P}}$

$$\mathbf{b} = \begin{bmatrix} \mathbf{b}_1 \\ \mathbf{b}_2 \\ \mathbf{b}_3 \\ \mathbf{b}_4 \\ \mathbf{b}_5 \\ \mathbf{b}_6 \end{bmatrix} = \begin{bmatrix} (\bar{\mathbf{1}} + \mathbf{h}_1)N_{I,1} \\ \mathbf{h}_2 N_{I,2} \\ (\bar{\mathbf{1}} + \mathbf{h}_1)N_{I,2} + \mathbf{h}_2 N_{I,1} \\ \mathbf{h}_3 N_{I,1} \\ (\bar{\mathbf{1}} + \mathbf{h}_4)N_{I,2} \\ (\bar{\mathbf{1}} + \mathbf{h}_3)N_{I,1} + \mathbf{h}_3 N_{I,2} \end{bmatrix} \in \mathbb{R}^{6\times \bar{P}}$$

$\mathbf{B}_I = \text{PCaug}(\mathbf{b}, 3, 2, \mathbf{M})$

end

The nodal contribution of the vector of internal forces $\mathbf{f}_I \in \mathbb{R}^{2\bar{P}\times 1}$ is computed in Algorithm 13 and subsequently assembled into $\mathbf{f}^e$, see Algorithm 7.

In Algorithm 14 the nodal contribution $\mathbf{k}_{TIK} \in \mathbb{R}^{2\bar{P}\times 2\bar{P}}$ of the element tangent stiffness matrix $\mathbf{k}_T^e$ is calculated. As can be seen, due to the geometrically nonlinear formulation, the matrix $\mathbf{k}_{TIK}$ comprises two parts. The first corresponds to the material part and the second to the geometric part, respectively.

Algorithm 13 Internal forces / Residual vector

Input: $\mathbf{B}_I \in \mathbb{R}^{3\bar{P}\times 2\bar{P}}$, $\mathbf{S} \in \mathbb{R}^{3\bar{P}\times 1}$, $\det \mathbf{J}$, w_{gp}

Output: $\mathbf{f}_I \in \mathbb{R}^{2\bar{P}\times 1}$

function $[\mathbf{f}_I] = \mathrm{Fint}(\mathbf{B}_I, \mathbf{S}, \det \mathbf{J}, w_{gp})$

$\mathbf{f}_I = \mathbf{B}_I^T \mathbf{S} \det \mathbf{J} w_{gp}$

end

Algorithm 14 Tangent stiffness matrix

Input: $\mathbf{B}_I, \mathbf{B}_K \in \mathbb{R}^{3\bar{P}\times 2\bar{P}}$, $\mathbf{C} \in \mathbb{R}^{3\bar{P}\times 3\bar{P}}$, $\mathbf{S} \in \mathbb{R}^{3\bar{P}\times 1}$, $\mathbf{N} \in \mathbb{R}^{2\times 4}$

$\mathbf{M} \in \mathbb{R}^{\bar{P}^2\times \bar{P}}$, $\det \mathbf{J}$, w_{gp}

Output: $\mathbf{k}_{TIK} \in \mathbb{R}^{2\bar{P}\times 2\bar{P}}$

function $[\mathbf{k}_{TIK}] = \mathrm{Tang}(\mathbf{B}_I, \mathbf{B}_K, \mathbf{C}, \mathbf{S}, \mathbf{N}, \mathbf{M}, \det \mathbf{J}, w_{gp})$

$\mathbf{i}_1 = [1, 3, \ldots, 3\bar{P}] \in \mathbb{R}^{1\times \bar{P}}$, $\mathbf{i}_2 = \mathbf{i}_1 + 1$, $\mathbf{i}_3 = \mathbf{i}_2 + 1$

$\mathbf{s}_{11} = \mathbf{S}(\mathbf{i}_1)$, $\mathbf{s}_{22} = \mathbf{S}(\mathbf{i}_2)$, $\mathbf{s}_{12} = \mathbf{S}(\mathbf{i}_3)$

$\mathbf{g} = (N_{I,1}N_{K,1})\mathbf{s}_{11} + (N_{I,2}N_{K,2})\mathbf{s}_{22} + (N_{I,1}N_{K,2} + N_{I,2}N_{K,1})\mathbf{s}_{22}$

$\mathbf{G} = \mathrm{vec}^{-1}_{\bar{P},\bar{P}}(\mathbf{g}^T\mathbf{M})$, $\mathbf{G}_{IK} = \mathbf{G} \otimes \mathbf{1}_{2\times 2}$

$\mathbf{k}_{TIK} = (\mathbf{B}_I^T \mathbf{C} \mathbf{B}_K + \mathbf{G}_{IK}) \det \mathbf{J} w_{gp}$

end

Since the symmetry of the element stiffness matrix is still preserved, it is sufficient to determine the lower diagonal of $\mathbf{k}_T^e$. In this case, the second loop over the nodes K runs from 1 to I.

D Layered cylindrical shell: Convergence of the MCS and the SSFEM

In the following, the convergence behavior of the MCS and the SSFEM is examined in more detail. For this purpose, we consider the stochastic attributes of the load factor λ, see Sect. 7.1.1. The percentage error $\varepsilon_{(\bullet)}$ of a quantity $(\bullet)$ refers to the reference solution of the MCS with $N = 5 \times 10^5$ samples and is given by

$$\varepsilon_{(\bullet)} = \frac{|(\bullet) - (\bullet)_{\mathrm{mcs5e5}}|}{|(\bullet)_{\mathrm{mcs5e5}}|} \cdot 100\,\% \,. \tag{121}$$

For the investigations, we consider the stochastic load factor λ at the displacement level $w = 15\,\mathrm{mm}$. Three independent runs of an MCS are performed, which are illustrated in Figs. 33, 34, and 35 with solid lines. In order to evaluate the convergence behavior of the MCS, the number of sample points N is successively increased from 10^2 to 10^5. To this end, additional samples are added to the original set of 10^2 realizations. The percentage errors of the SSFEM results are determined according to Eq. (121). These are shown as dashed horizontal lines in the Figs. 33, 34, and 35.

Figure 33 shows that a percentage error of less than 1 % can be achieved for the mean value μ_λ with approximately 5×10^2 samples. For the SSFEM configuration sfem p1q1, the percentage error is below 1 %, whereas the other configurations exhibit even smaller deviations. The yellow dashed line corresponding to sfem p4q0.8 obscures the green dashed line, which corresponds to sfem p3q1.

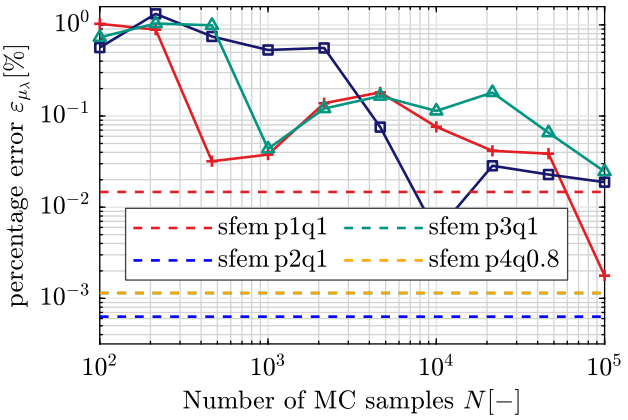

Fig. 33 Percentage error $\varepsilon_{\mu_\lambda}$ of the mean value μ_λ of the load factor λ at the displacement level $w = 15\,\mathrm{mm}$

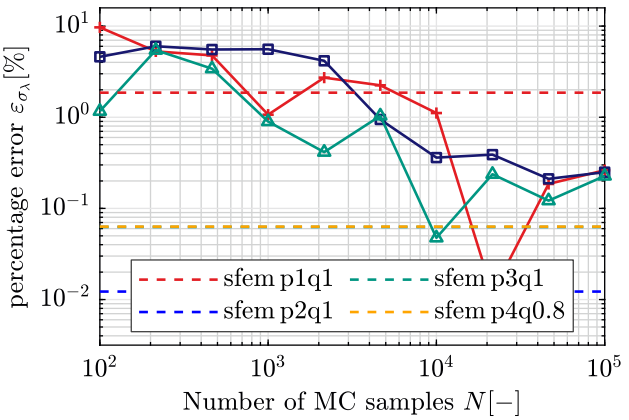

Fig. 34 Percentage error $\varepsilon_{\sigma_\lambda}$ of the standard deviation σ_λ of the load factor λ at the displacement level $w = 15\,\mathrm{mm}$

A similar trend of the percentage errors can be observed for the standard deviation σ_λ, see Fig. 34. Overall, it can be seen that the standard deviation converges slower than the mean value. In Fig. 34, the green dashed line of sfem p3q1 is obscured by the yellow dashed line of sfem p4q0.8.

Considering Figs. 33 and 34, it is also apparent that the SSFEM results of the configuration sfem p2q1 show a slightly lower error than those of sfem p3q1 and sfem p4q0.8. This can be explained by the fact that even when using 5×10^5 samples for the MCS reference solution, minimal fluctuations in the stochastic moments can occur. This is not the case with an analytical solution. Here, a continuous improvement in the SSFEM results would be noticeable as the polynomial degree increases.

Figure 35 depicts the skewness δ_λ of load factor λ. It becomes clear that this stochastic attribute converges more

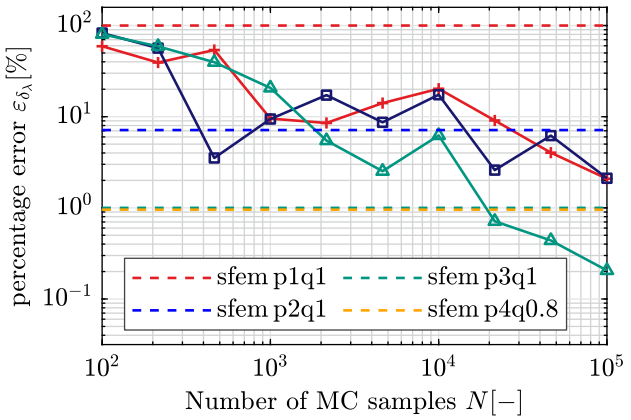

Fig. 35 Percentage error $\varepsilon_{\delta_\lambda}$ of the skewness δ_λ of the load factor λ at the displacement level $w = 15\,\text{mm}$

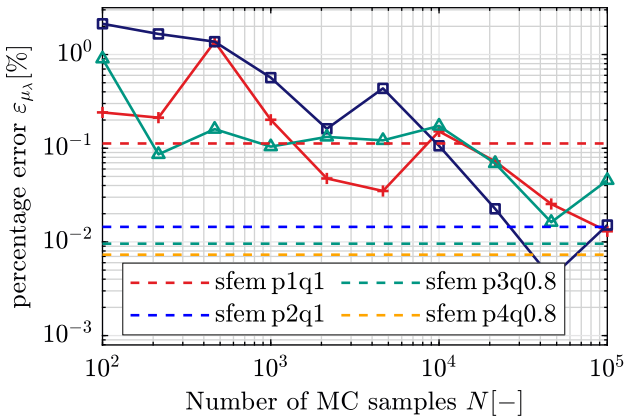

Fig. 36 Percentage error $\varepsilon_{\mu_\lambda}$ of the mean value μ_λ of the load factor λ at the displacement level $w = 28\,\text{cm}$

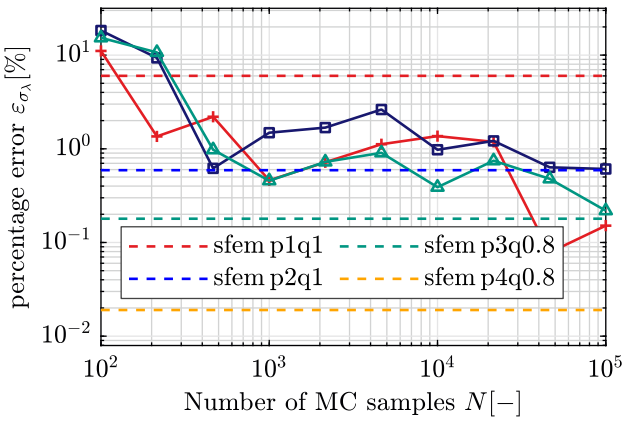

Fig. 37 Percentage error $\varepsilon_{\sigma_\lambda}$ of the standard deviation σ_λ of the load factor λ at the displacement level $w = 28\,\text{cm}$

slowly than the mean value μ_λ and the standard deviation σ_λ. The SSFEM configurations sfem p3q1 and sfem p4q0.8 result in errors of approximately 1% for the skewness of the load factor λ.

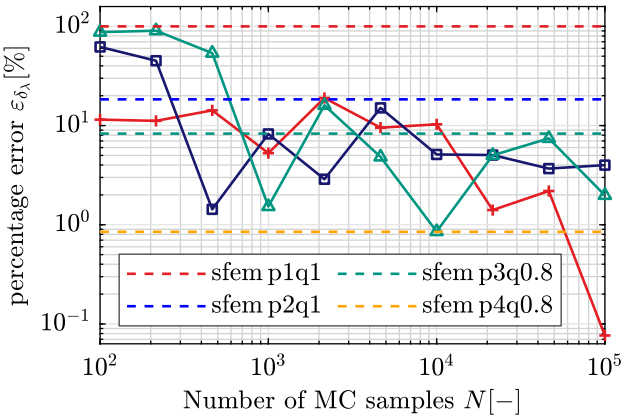

Fig. 38 Percentage error $\varepsilon_{\delta_\lambda}$ of the skewness δ_λ of the load factor λ at the displacement level $w = 28\,\text{cm}$

E Single-hinged frame: Convergence of the MCS and the SSFEM

In the following section, we analyze the convergence behavior of the MCS and the SSFEM in more detail. For the investigations, we consider the load factor λ at the displacement level $w = 28\,\text{cm}$. The convergence behavior of the MCS and the approximation quality of different SSFEM configurations is determined using the same procedure as described in Appendix D.

Figure 36 clearly shows the convergence of the mean value as the number of MC samples increases. Using a linear polynomial basis, the first stochastic moment μ_λ is captured with a percentage error of less than 1 %. Increasing the polynomial degree of the underlying PC expansion leads to a further reduction in the error $\varepsilon_{\mu_\lambda}$.

Figure 37 clearly illustrates the influence of the polynomial degree. Using higher-order polynomial bases improves the accuracy of the standard deviation σ_λ.

A similar convergence behavior of the SSFEM configurations is observed for the skewness δ_λ, see Fig. 38. For the MCS, it becomes clear that the third stochastic moment δ_λ converges more slowly than the first two stochastic attributes μ_λ and σ_λ. Consequently, more MC samples are necessary to achieve an error smaller than a defined error threshold.

Funding Open Access funding enabled and organized by Projekt DEAL.

References

1. Acharjee S, Zabaras N (2006) Uncertainty propagation in finite deformations-a spectral stochastic Lagrangian approach. Comput Methods Appl Mech Eng 195(19–22):2289–2312. https://doi.org/10.1016/j.cma.2005.05.005
2. Ammouche Y, Jérusalem A (2022) A modular nonlinear stochastic finite element formulation for uncertainty estimation. Comput Methods Appl Mech Eng 396:115044. https://doi.org/10.1016/j.cma.2022.115044
3. Arregui-Mena JD, Margetts L, Mummery PM (2014) Practical application of the stochastic finite element method. Arch Comput Methods Eng 23(1):171–190. https://doi.org/10.1007/s11831-014-9139-3
4. Batoz J, Dhatt G (1979) Incremental displacement algorithms for nonlinear problems. Int J Numer Methods Eng 14(8):1262–1267. https://doi.org/10.1002/nme.1620140811
5. Blatman G, Sudret B (2011) Adaptive sparse polynomial chaos expansion based on least angle regression. J Comput Phys 230(6):2345–2367. https://doi.org/10.1016/j.jcp.2010.12.021
6. Caflisch RE (1998) Monte Carlo and quasi-Monte Carlo methods. Acta Numer 7:1–49. https://doi.org/10.1017/S0962492900002804
7. Debusschere BJ, Najm HN, Pebay PP, Knio OM, Ghanem RG, Le Maître OP (2004) Numerical challenges in the use of polynomial chaos representations for stochastic processes. SIAM J Sci Comput 26(2):698–719. https://doi.org/10.1137/S1064827503427741
8. Ghanem RG, Spanos PD (1991) Stochastic Finite Elements: A Spectral Approach. Springer New York. https://doi.org/10.1007/978-1-4612-3094-6
9. Gruttmann F, Wagner W (2024) A FE2 shell model with periodic boundary conditions for thin and thick shells. Int J Numer Methods Eng. https://doi.org/10.1002/nme.7433
10. Le Maître OP, Knio OM (2010) Spectral Methods for Uncertainty Quantification: With Applications to Computational Fluid Dynamics. Springer Netherlands. https://doi.org/10.1007/978-90-481-3520-2
11. Lee SL, Manuel FS, Rossow EC (1968) Large deflections and stability of elastic frame. J Eng Mech Div 94(2):521–548. https://doi.org/10.1061/JMCEA3.0000966
12. Panther L (2025) Theorie und Numerik spektraler stochastischer Finite-Elemente-Formulierungen bei geometrisch nichtlinearem Deformationsverhalten, Dissertation, Institut für Baustatik, Karlsruher Institut für Technologie. https://doi.org/10.5445/IR/1000191022
13. Panther L, Wagner W, Freitag S (2025) A consistently linearized spectral stochastic finite element formulation for geometric nonlinear composite shells. Comput Mech 75(5):1655–1683. https://doi.org/10.1007/s00466-024-02583-0
14. Papadopoulos V, Kalogeris I, Giovanis DG (2019) A spectral stochastic formulation for nonlinear framed structures. Probab Eng Mech 55:90–101. https://doi.org/10.1016/j.probengmech.2018.11.002
15. Pian THH, Sumihara K (1984) Rational approach for assumed stress finite elements. Int J Numer Methods Eng 20(9):1685–1695. https://doi.org/10.1002/nme.1620200911
16. Reissner E (1972) On one-dimensional finite-strain beam theory: the plane problem. Zeitschrift für angewandte Mathematik und Physik ZAMP 23(5):795–804. https://doi.org/10.1007/BF01602645
17. Soize C, Ghanem R (2004) Physical systems with random uncertainties: chaos representations with arbitrary probability measure. SIAM J Sci Comput 26(2):395–410. https://doi.org/10.1137/S1064827503424505
18. Stefanou G (2009) The stochastic finite element method: past, present and future. Comput Methods Appl Mech Eng 198(9–12):1031–1051. https://doi.org/10.1016/j.cma.2008.11.007
19. Sudret B (2000) Stochastic finite element methods and reliability: a state-of-the-art report. University of California, Berkeley
20. Sudret B (2008) Global sensitivity analysis using polynomial chaos expansions. Reliab Eng Syst Saf 93(7):964–979. https://doi.org/10.1016/j.ress.2007.04.002
21. Sudret B (2014) Polynomial Chaos Expansions and Stochastic Finite Element Methods. CRC Press, 265-300
22. Taylor RL (2025) FEAP-Finite Element Analysis Program. University of California, Berkeley. http://projects.ce.berkeley.edu/feap/
23. The MathWorks Inc (2021) Matlab version: 9.10.0 R2021a. Tech. rep., Natick, Massachusetts. https://www.mathworks.com
24. Wagner W (1990) A finite element model for non-linear shells of revolution with finite rotations. Int J Numer Methods Eng 29(7):1455–1471. https://doi.org/10.1002/nme.1620290706
25. Wagner W, Wriggers P (1988) A simple method for the calculation of postcritical branches. Eng Comput 5(2):103–109. https://doi.org/10.1108/eb023727
26. Wiener N (1938) The homogeneous chaos Am J Math 60(4):897. https://doi.org/10.2307/2371268
27. Wriggers P (2008) Nonlinear Finite Element Methods. Springer New York. https://doi.org/10.1007/978-3-540-71001-1
28. Xiu D, Karniadakis GE (2002) The Wiener-Askey polynomial chaos for stochastic differential equations. SIAM J Sci Comput 24(2):619–644. https://doi.org/10.1137/S1064827501387826
29. Xiu D, Karniadakis GE (2003) Modeling uncertainty in flow simulations via generalized polynomial chaos. J Comput Phys 187(1):137–167. https://doi.org/10.1016/S0021-9991(03)00092-5